Influences of Time-Dependent Precipitation on Water Mass Transformation, Heat Fluxes, and Deep Convection in Marginal Seas

YUKI YASUDA

Department of Earth and Planetary Science, University of Tokyo, Tokyo, Japan

MICHAEL A. SPALL

Department of Physical Oceanography, Woods Hole Oceanographic Institution, Woods Hole, Massachusetts

(Manuscript received 22 July 2014, in final form 2 April 2015)

ABSTRACT

Influences of time-dependent precipitation on water mass transformation and heat budgets in an idealized marginal sea are examined using theoretical and numerical models. The equations proposed by Spall in 2012 are extended to cases with time-dependent precipitation whose form is either a step function or a sinusoidal function. The theory predicts the differences in temperature and salinity between the convective water and the boundary current as well as the magnitudes of heat fluxes into the marginal sea and across the sea surface. Moreover, the theory reveals that there are three inherent time scales: relaxation time scales for temperature and salinity and a precipitation time scale. The relaxation time scales are determined by a steady solution of the theoretical model with steady precipitation. The relaxation time scale for temperature is always smaller than that for salinity as a result of not only the difference in the form of fluxes at the surface but also the variation in the eddy transport from the boundary current. These three time scales and the precipitation amplitude determine the strength of the ocean response to changes in precipitation and the phase relation between precipitation, changes in salinity and temperature, and changes in heat fluxes. It is demonstrated that the theoretical predictions agree qualitatively well with results from the eddy-resolving numerical model. This demonstrates the fundamental role of mesoscale eddies in the ocean response to time-dependent forcing and provides a framework with which to assess the extent to which observed variability in marginal sea convection and water mass transformation are consistent with an external forcing by variations in precipitation.

1. Introduction

The oceanic thermohaline circulation plays an important role in the global heat budget and hydrological cycle by transporting heat from low to high latitudes and freshwater from high to low latitudes. Marginal seas (e.g., Labrador Sea, Mediterranean Sea, and Greenland Sea) are especially important for the thermohaline circulation because they are one of the primary origins of the deep-ocean water (e.g., Pickart et al. 2002) that spreads widely throughout the ocean (Talley and McCartney 1982).

A marginal sea can be roughly divided into an interior and a boundary region, which are designated as light blue and orange, respectively, in Fig. 1. In the boundary region, there is a strong, surface-intensified current along the bottom topography, while there is deep convection in the interior with weak (horizontal) mean flows, as shown by direct velocity measurements of $O(1)\,\mathrm{cm\,s^{-1}}$ in the Labrador Sea (Lavender et al. 2000). Exchange between the two regions is regulated by baroclinic eddies (e.g., Khatiwala and Visbeck 2000; Lilly and Rhines 2002; Lilly et al. 2003; Spall 2004). Buoyancy loss in the boundary current, due to eddies and atmospheric cooling, decreases the baroclinic transport along the perimeter (Walin et al. 2004; Spall 2004). This barotropization of the current requires a net downwelling. This downwelling can occur either in a barotropic coastal current (Walin et al. 2004) or directly in the baroclinic boundary current (Spall 2010; Cenedese 2012). In the interior, there may be many plumes where there is strong downwelling; however, the mean downwelling is quite small because of the compensatory upwelling (Schott et al. 1993; Send and Marshall 1995; Marshall and Schott

Corresponding author address: Yuki Yasuda, Department of Earth and Planetary Science, University of Tokyo, 7-3-1 Hongo, Bunkyo-ku, Tokyo 113-0033, Japan.
E-mail: yyuuki@eps.s.u-tokyo.ac.jp

DOI: 10.1175/JPO-D-14-0147.1

© 2015 American Meteorological Society

1999); the mean vertical velocity is less than 0.1 mm s^{-1} by scaling arguments with the vorticity equation.

One method for analyzing the thermohaline circulation is to use a simplified system such as the two-box model of Stommel (1961). In this model, one box designates the low-latitude ocean, while the other designates the high-latitude ocean. The exchange between the two boxes is due to the mean flow directly driven by the pressure gradient. Such simplified systems allow for nondimensional analytic solutions that make parameter dependencies and inherent physics clearer.

Recently, several studies have proposed simplified models for marginal seas (e.g., Spall 2004, 2011, 2012; Walin et al. 2004; Straneo 2006; Wahlin and Johnson 2009; Born and Stocker 2014). Spall (2012) derived a new simplified system [referred to here as the dynamical system (DS)] with a steady heat and freshwater flux forcing. The governing equations of the DS are similar to those of Stommel, but the model physics differ in important ways. The most essential difference is that the exchange between the two boxes is due not to the mean flow but to baroclinic eddies. The DS predicts the properties of convective water and the strength of meridional overturning circulation as well as the magnitude of precipitation required to shut down deep convection. Spall's theory was supported by comparing the theoretical predictions with the results from a numerical model in which mesoscale eddies were explicitly resolved.

Several studies have shown that excess precipitation may lead to a reduction in the formation of deep-ocean water, the meridional heat transport, and the strength of meridional overturning circulation (e.g., Rahmstorf 1995; Rahmstorf et al. 2005; Spall 2012). In the present paper, we focus on time-dependent precipitation and examine responses of the marginal sea by using a time-dependent version of the DS proposed by Spall (2012). Two kinds of precipitation are considered: a step function and a sinusoidal function. A superposition of these forcings can produce any time-dependent forcing so that the present study gives typical examples of the responses of marginal seas to changes in precipitation. This idealized approach also allows for a clear demonstration of the controlling physics and inherent time scales of the problem. The basic predictions from the DS are tested by comparison with results from an eddy-resolving numerical model.

The structure of the paper is as follows: In section 2, the DS with time-dependent precipitation is examined by a linear system derived from the DS. We compare the relaxation time scales for temperature and salinity given by the linear system with those obtained by Wahlin and Johnson (2009). In section 3, the predictions from the DS are compared with quantities diagnosed from eddy-resolving numerical model simulations. Finally, in section 4, the results are summarized.

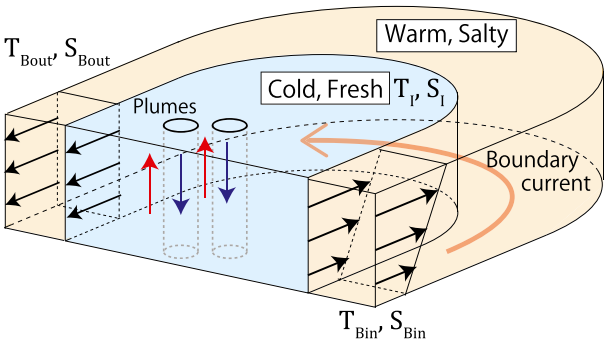

FIG. 1. Schematic illustration of the marginal sea for the thermal mode, in which seawater in the interior is denser than that in the boundary current and the boundary current is cyclonic. Here, the convective region (light blue) is referred to as the interior or interior region, while the surrounding region (orange) is referred to as boundary current or boundary region. The entire region (i.e., the sum of the interior and the boundary current) is called the basin. See text for details.

2. Dynamical system with time-dependent precipitation

a. *Extension of the DS proposed by Spall (2012)*

We examine temperature and salinity of convective water masses by the simplified dynamical system proposed by Spall (2012). This DS predicts differences in temperature and salinity between a boundary current and a convective interior in an idealized marginal sea, which are designated as orange and light blue in Fig. 1, respectively. The temperature and salinity fluxes between the two regions are regulated by baroclinic eddies. We further made the following four assumptions: (i) Baroclinic eddy fluxes are parameterized as $\overline{v'T'} = cV(T_{Bin} - T_I)$, where $\overline{v'T'}$ is the average of eddy temperature fluxes, V is a scale for the alongfront velocity; T_{Bin} is the temperature of the inflowing boundary current; T_I is the temperature averaged over the interior; and c is a nondimensional constant that reflects the strength of eddy fluxes resulting from baroclinic instability (Spall 2004). Note that c includes the stabilization effect due to the bottom slope and is fixed to be 0.007 as in Spall (2012). (ii) For the purposes of parameterizing baroclinic instability, temporal and spatial variation in the boundary current can be ignored, that is, T_{Bin} and S_{Bin} are constant, where S_{Bin} is the salinity of the inflowing boundary current. (iii) The scale V is obtained by the thermal wind equation [(3)]. (iv) The interior is always horizontally and vertically uniform. The symbols and notations used in the present paper are summarized in Table 1. The configuration of the

TABLE 1. Symbols and notations used in the present paper. A quantity with a star represents the corresponding dimensional quantity.

Symbol	Definition	Fixed value	Units
$T_{\rm Bin}$ ($T_{\rm Bout}$)	Temperature of the inflowing (outflowing) boundary current	— (—)	°C (°C)
$S_{\rm Bin}$ ($S_{\rm Bout}$)	Salinity of the inflowing (outflowing) boundary current	— (—)	ppt (ppt)
$T_{\rm I}$	Temperature of the interior	—	°C
$S_{\rm I}$	Salinity of the interior	—	ppt
V	Scale for the alongfront velocity defined in (3)	—	$\mathrm{m\,s^{-1}}$
Γ	Relaxation constant of heat fluxes across the sea surface	10	$\mathrm{W\,m^{-2}\,°C^{-1}}$
E_0	Constant freshwater flux	-2×10^{-8}	$\mathrm{m\,s^{-1}}$
$E'(t)$	Time-dependent freshwater flux	—	$\mathrm{m\,s^{-1}}$
$t(t^\star)$	Nondimensional (dimensional) time	— (—)	— (s)
H_0	Averaged depth of the interior	2000	m
A	Surface area of the interior	—	$\mathrm{m^2}$
P	Perimeter of the interior	—	m
$H_{\rm sill}$	Sill depth	1000	m
ρ_0	Representative density	1000	$\mathrm{kg\,m^{-3}}$
S_0	Representative salinity	35	ppt
C_p	Specific heat	4000	$\mathrm{J\,kg^{-1}\,°C^{-1}}$
$T_{\rm A}$	Atmospheric temperature averaged over the interior	—	°C
g	Gravitational acceleration	9.8	$\mathrm{m\,s^{-2}}$
f_0	Reference Coriolis parameter	1×10^{-4}	$\mathrm{s^{-1}}$
L	Width of the sloping topography	75×10^{3}	m
α_T	Thermal expansion coefficient	0.2	$\mathrm{kg\,m^{-3}\,°C^{-1}}$
α_S	Haline expansion coefficient	0.8	$\mathrm{kg\,m^{-3}}$
T^*	$T_{\rm Bin}-T_{\rm A}$	6.2	°C
N^2	Squared buoyancy frequency	2×10^{-6}	$\mathrm{s^{-2}}$
c	Strength of parameterized eddy fluxes (e.g., $\overline{v'T'}=cV(T_{\rm Bin}-T_{\rm I})$)	0.007	—
ΔT	$(T_{\rm Bin}-T_{\rm I})/T^*$	—	—
ΔS	$(S_{\rm Bin}-S_{\rm I})\alpha_S/(\alpha_T T^*)$	—	—
τ	Characteristic time scale for nondimensionalization defined in (6)	3.2	yr
ϵ	Eq. (7)	0.18	—
μ	Eq. (7)	1.1×10^{-2}	—
γ_0	Eq. (7)	-1.6×10^{-2}	—
$\gamma'(t)$	Obtained by replacing E_0 in γ_0 with $E'(t)$	—	—
$\Delta\gamma'$	Magnitude of $\gamma'(t)$ [$=\Delta\gamma'\Theta(t)$ or $\Delta\gamma'\sin(\omega t)$]	—	—
$\Theta(t)$	Heaviside step function [$\Theta=1$ ($t\ge0$) and 0 ($t<0$)]	—	—
$\omega(\omega^\star)$	Nondimensional (dimensional) frequency	— (—)	— ($\mathrm{yr^{-1}}$)
$\Delta T_{\rm s}$ and $\Delta S_{\rm s}$	Steady thermal-mode solution of the DS without $\gamma'(t)$	—	—
$\Delta T'(t)$ and $\Delta S'(t)$	Perturbations from $\Delta T_{\rm s}$ and $\Delta S_{\rm s}$ (or time-averaged values)	—	—
$\Delta\rho_{\rm s}$	$\Delta T_{\rm s}-\Delta S_{\rm s}$	—	—
$\Delta\rho'(t)$	$\Delta T'(t)-\Delta S'(t)$	—	—
$\tau_T(\tau_T^\star)$	Relaxation time scale for $\Delta T'$, $\tau_T\equiv(2\mu/\epsilon+\Delta\rho_{\rm s}+\Delta T_{\rm s})^{-1}$	1.4 (4.5)	— (yr)
$\tau_S(\tau_S^\star)$	Relaxation time scale for $\Delta S'$, $\tau_S\equiv\Delta\rho_{\rm s}^{-1}$	4.1 (12.9)	— (yr)
t_0	Nondimensional initial time	—	—
C	$-\Delta\gamma'/(4\epsilon)$	—	—
ϕ_T	$\tan^{-1}(\omega\tau_T)$	—	—
ϕ_S	$\tan^{-1}(\omega\tau_S)$	—	—
$\mathrm{HF_{surf}}(\mathrm{HF_{surf}^\star})$	Eq. (16)	— (—)	— ($\mathrm{J\,s^{-1}}$)
$\mathrm{HF_{sill}}(\mathrm{HF_{sill}^\star})$	Eq. (18)	— (—)	— ($\mathrm{J\,s^{-1}}$)
$\Delta T_{\rm ave}$ and $\Delta S_{\rm ave}$	Time-averaged ΔT and ΔS over one period (sine function case)	—	—
$\Delta T_{\rm AT}$, $\Delta S_{\rm AT}$, and $\Delta\rho_{\rm AT}$	Time-averaged ΔT, ΔS, and $\Delta\rho$ over the last 20 yr (step function case)	—	—

idealized marginal sea (Fig. 1) and the assumption iv are supported by observations (e.g., Lavender et al. 2000; Lazier et al. 2002; Pickart et al. 2002), while the other assumptions i–iii are supported by numerical simulations (e.g., Spall 2011, 2012).

Two kinds of atmospheric forcing are considered: heat and freshwater fluxes across the sea surface. The heat flux is parameterized by a relaxation of the sea surface temperature toward an atmospheric temperature with a relaxation constant Γ (Haney 1971). The freshwater flux (evaporation minus precipitation) can be specified as $E_0+E'(t)$, where E_0 is constant and $E'(t)$ is time dependent. Unlike for heat flux, there is no feedback between the sea surface salinity and the freshwater flux.

Huang (1993) showed that such a virtual salt flux boundary condition can result in significant errors when the surface salinity is far from the mean surface salinity and advocates for the use of a more realistic freshwater flux through the surface. However, the surface salinity in the basin is never far from its mean value in the present study and our simplified approach allows for relatively simple analytic solutions and interpretation of the controlling physics. Note that wind stress is not included in the DS, but it is included in the numerical model in section 3.

Temperature and salinity equations spatially integrated over the interior are obtained as follows:

$$H_0 A \frac{dT_\mathrm{I}}{dt^\star} = PH_\mathrm{sill} cV(T_\mathrm{Bin} - T_\mathrm{I}) - \frac{A\Gamma(T_\mathrm{I} - T_\mathrm{A})}{\rho_0 C_p}, \quad \text{and} \tag{1}$$

$$H_0 A \frac{dS_\mathrm{I}}{dt^\star} = PH_\mathrm{sill} cV(S_\mathrm{Bin} - S_\mathrm{I}) + AS_0[E_0 + E'(t)], \tag{2}$$

where $t^\star$ is time; S_I is the salinity averaged over the interior; H_0 is the averaged depth of the interior; A is the surface area of the interior; P is the perimeter of the interior where the topography is flat or the topographic contours are closed; H_sill is the sill depth between the marginal sea and the open ocean; ρ_0 is a representative ocean density; C_p is the specific heat of seawater; T_A is the atmospheric temperature spatially averaged over the interior; and S_0 is a representative salinity. Equations (1) and (2) describe the time evolution of temperature and salinity in the interior, respectively, which are changed by baroclinic eddy fluxes confined above the sill depth and by the atmospheric forcing at the sea surface. The boundary current is roughly confined above the sill depth (Spall 2004; Walin et al. 2004) and hence baroclinic eddy fluxes from the boundary current are also concentrated there.

The characteristic velocity V is given by the thermal wind equation (assumption iii) following Spall (2012):

$$\begin{aligned} V &= \frac{gH_\mathrm{sill}}{2\rho_0 f_0 L}[\alpha_T(T_\mathrm{Bin} - T_\mathrm{I}) - \alpha_S(S_\mathrm{Bin} - S_\mathrm{I})] \\ &= \frac{gH_\mathrm{sill}}{2\rho_0 f_0 L}\alpha_T T^*(\Delta T - \Delta S), \end{aligned} \tag{3}$$

where g is the gravitational acceleration; f_0 is the reference Coriolis parameter; L is the width of the sloping topography over which the boundary current lies; α_T is the thermal expansion coefficient ($\mathrm{kg\,m^{-3}\,{}^\circ C^{-1}}$); and α_S is the haline expansion coefficient ($\mathrm{kg\,m^{-3}}$). Note that a linear equation of state is used. Quantities of ΔT and ΔS are the nondimensionalized differences in temperature and salinity between the interior and the boundary current, respectively: $\Delta T \equiv (T_\mathrm{Bin} - T_\mathrm{I})/T^*$ and $\Delta S \equiv (S_\mathrm{Bin} - S_\mathrm{I})\alpha_S/(\alpha_T T^*)$, where $T^* = T_\mathrm{Bin} - T_\mathrm{A}$.

Using (1), (2), and (3), we obtain the nondimensional equations for ΔT and ΔS:

$$\frac{d}{dt}\Delta T = -\Delta T|\Delta T - \Delta S| + \frac{2\mu}{\epsilon}(1 - \Delta T), \quad \text{and} \tag{4}$$

$$\frac{d}{dt}\Delta S = -\Delta S|\Delta T - \Delta S| - \frac{\gamma_0 + \gamma'(t)}{4\epsilon}, \tag{5}$$

where t is nondimensional time. Note that a quantity with a star is the corresponding dimensional quantity, for example, $t^\star$. Time is nondimensionalized by the characteristic time scale

$$\tau \equiv \frac{H_0 A}{PH_\mathrm{sill}} \frac{1}{c} \frac{2\rho_0 f_0 L}{gH_\mathrm{sill}\alpha_T T^*}. \tag{6}$$

Nondimensional parameters ϵ, μ, and γ_0 are constant, while γ' represents the nondimensional time-dependent precipitation:

$$\epsilon \equiv \frac{cP}{L}, \quad \mu \equiv \frac{A\Gamma f_0}{\alpha_T g C_p H_\mathrm{sill}^2 T^*}, \quad \gamma_0 \equiv \frac{8A\rho_0 f_0 S_0 \alpha_S E_0}{gH_\mathrm{sill}^2 \alpha_T^2 T^{*2}}. \tag{7}$$

The value of $\gamma'(t)$ is obtained by replacing E_0 in γ_0 with $E'(t)$. The DS consists of (4) and (5) with (7), which is the same as in Spall (2012) except for the time derivative terms and $\gamma'(t)$. The factor ϵ represents the ratio of the inflowing water fluxed into the interior by eddies $cVPH_\mathrm{sill}$ to that in the boundary current VLH_sill. The constant μ/ϵ characterizes the balance between the surface heat flux and the eddy heat fluxes, while γ/ϵ characterizes the balance between the surface freshwater flux and the eddy salinity fluxes (Spall 2011, 2012). A new parameter τ characterizes the time it takes to flush the interior by eddies, similar to that in Straneo (2006).

In the present paper, two forms of $\gamma'(t)$ are considered: the Heaviside step function $\Delta\gamma'\Theta(t)$ and the sine function $\Delta\gamma'\sin(\omega t)$. A superposition of these two types of forcing can produce any time-dependent forcing, so that the results obtained here are typical examples of the response of marginal seas to changes in precipitation. Amplitudes and frequencies of γ' will be varied, while ϵ, μ, and γ_0 are fixed to be 0.18, 1.1×10^{-2}, and -1.6×10^{-2}, respectively, as is appropriate for the marginal seas in the subpolar North Atlantic (Labrador Sea and Greenland Sea; Spall 2012). The range of $\Delta\gamma'$ is between $\pm 0.4\gamma_0$ for the step function and $\pm\gamma_0$ for the sine function. The maximum precipitation considered in the present paper is $2\gamma_0$. The stable thermal mode still exists in the DS with the doubled steady precipitation ($\gamma_0 \to 2\gamma_0$ and $\gamma' = 0$); however, this value is close to what is required to shut down deep convection (Spall 2012). It is beyond the present paper to examine the DS with γ' whose amplitude is large enough to cause the shutdown of deep convection. The period of the sine

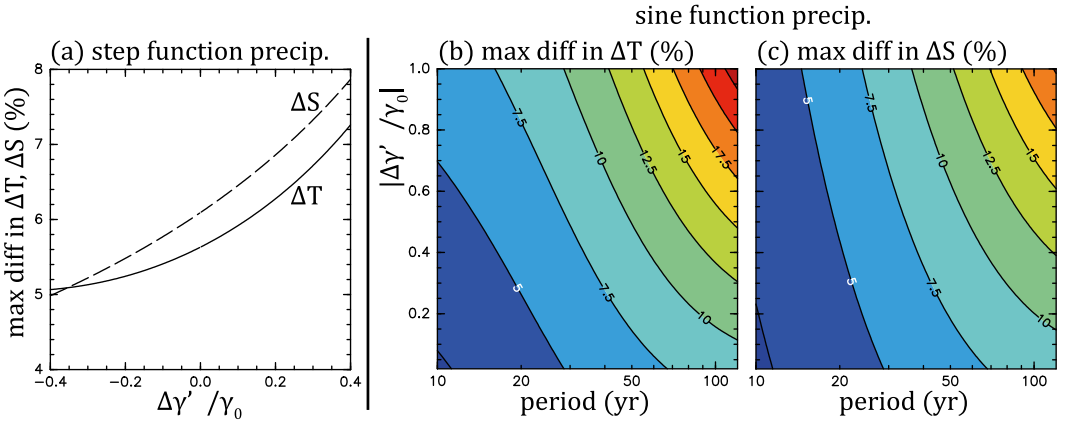

FIG. 2. (a) The maximum differences in ΔT and ΔS between the DLEs and the DS for the step function precipitation [$\gamma'(t) = \Delta\gamma'\Theta(t)$]. (b),(c) As in (a), but for the maximum differences in (b) ΔT and (c) ΔS for sine function precipitation [$\gamma'(t) = \Delta\gamma' \sin(\omega t)$]. Each maximum difference is normalized by a difference in the DS solution between the maximum and the minimum. The contour interval (CI) is 2.5% in (b) and (c).

function is varied between 10 and 120 yr (3.17 and 38.0 in nondimensional numbers). The initial condition is taken to be the steady solution with $\gamma' = 0$. All solutions in the above parameter space (i.e., ω–$\Delta\gamma'$ space) are limit cycles that attract nearby points. Solutions with different initial values approach the same periodic solution (not shown in detail). Thus, a phase constant in γ' is not considered.

b. *Decoupled linear equations*

Equations (4) and (5) are still complicated because they are nonlinear and coupled. If they are linearized around a steady solution, the resulting linear equations are still coupled. In the stable thermal mode, $1 > \Delta T_s > \Delta\rho_s > \Delta S_s > 0$, where a subscript s denotes a steady solution with steady precipitation and $\Delta\rho_s \equiv \Delta T_s - \Delta S_s$. This inequality means that the seawater in the boundary current is warmer and saltier than that in the interior, as in Fig. 1. Ignoring the smallest linear term proportional to ΔS_s in (5), we obtain the decoupled linear equations (DLEs) from (4) and (5):

$$\frac{d}{dt}\Delta T' = -\Delta T_s \Delta\rho' - \Delta T'\Delta\rho_s - \frac{2\mu}{\epsilon}\Delta T' = -\frac{1}{\tau_T}\Delta T' + \Delta T_s \Delta S', \quad \text{and} \tag{8}$$

$$\frac{d}{dt}\Delta S' = -\Delta S'\Delta\rho_s - \frac{\gamma'(t)}{4\epsilon} = -\frac{1}{\tau_S}\Delta S' - \frac{\gamma'(t)}{4\epsilon}, \tag{9}$$

where a perturbation is denoted by a prime and $\Delta\rho' \equiv \Delta T' - \Delta S'$ (i.e., $\Delta T = \Delta T_s + \Delta T'$ and the same for ΔS and $\Delta\rho$). Relaxation time scales for temperature and salinity are $\tau_T \equiv (2\mu/\epsilon + \Delta\rho_s + \Delta T_s)^{-1}$ and $\tau_S \equiv \Delta\rho_s^{-1}$, respectively. It is worth noting that τ_T is always smaller than τ_S. The temperature relaxation time scale is influenced by the restoration of the atmospheric temperature ($2\mu/\epsilon$ in τ_T), the anomalous eddy flux resulting from density anomalies (ΔT_s in τ_T), and the anomalous eddy flux resulting from temperature anomalies ($\Delta\rho_s$ in τ_T). In contrast, the salinity relaxation time scale results only from salinity anomalies carried by the mean density anomaly. A steady solution for a sine function forcing is obtained by solving (4) and (5) with $\gamma' = 0$, while one for a step function is obtained by solving with $\gamma_0 + \Delta\gamma$(const). In other words, a new steady state after transition at $t = 0$ is used to construct the DLEs with the step function precipitation, which means that the forcing $\gamma'(t)$ is replaced with $-\Delta\gamma'\Theta(-t)$ in (9).

The DLEs are evaluated by comparison to the solution of the DS, where the initial condition is the equilibrium without time-dependent precipitation. The DLEs and DS are solved by the fourth-order Runge–Kutta method. A nondimensional time step is 2×10^{-3} ($\approx 2 \times 10^5$ s) for step function precipitation, while it is chosen for a sine function such that one period is equally divided by 6000. Note that the results are not sensitive to the above choice of time step. Figure 2 shows the maximum differences in ΔT and ΔS between the DS and the DLEs that are normalized by the maximum variations in respective DS solutions. It is found that the DLEs can reproduce the DS solution within $O(10\%)$ accuracy in all parameter space considered in the present paper. In the step function case (Fig. 2a), the difference is asymmetric about the sign of $\Delta\gamma'/\gamma_0$, which may reflect the asymmetry of the transition time scale discussed in section 3b. In the sine function case (Figs. 2b,c), the difference tends to be large as the precipitation period or amplitude is large. This tendency likely reflects the fact that the interior can strongly respond to changes in precipitation when the precipitation

period or amplitude is large. This point is further discussed in sections 2b(2) and 2c.

Equations (8) and (9) indicate that there are three time scales inherent in the idealized marginal sea. The first time scale is the relaxation time scale τ_T for $\Delta T'$ in (8), which consists of the atmospheric cooling and part of the eddy temperature fluxes. The second one is the relaxation time scale τ_S for $\Delta S'$ in (9), which is equal to the eddy flushing time scale. The term proportional to $-1/\tau_T$ or $-1/\tau_S$ reduces a perturbation and forces the state to equilibrium without time-dependent precipitation. The third time scale may be given by $\gamma'(t)$. When precipitation is a sine function, $1/\omega$ is the third time scale, while it does not appear for a step function because the precipitation changes instantaneously. The dimensionalized time scales are obtained by multiplying by τ defined in (6): $\tau_S^\star = 12.9\,\text{yr}$ and $\tau_T^\star = 4.5\,\text{yr}$. Note again that a star indicates the corresponding dimensional quantity. It is worth noting that τ_S and τ_T are determined only by ϵ, μ, and γ_0 because both time scales are given by the DS solution without time-dependent precipitation.

The relaxation time scale for temperature is always smaller than that for salinity as in Wahlin and Johnson (2009). They argued that the difference in the surface flux boundary condition makes the temperature adjustment faster than that of salinity. However, there are four differences from their theory: First, they examined the structure of a steady boundary current in a marginal sea. This means that quantities obtained as their adjustment length scales divided by the velocity of the boundary current (the constant Q in their study) correspond to the relaxation time scales. Second, the surface freshwater flux is not proportional to S in (2), while it is in their theory. This difference makes the time-scale separation clearer, that is, τ_S becomes larger; the denominator of τ_S does not include a relaxation coefficient of the surface freshwater flux, and τ_S is simply controlled by the eddy dynamics, given by $\Delta\rho_s^{-1}$. The third and most important difference is that the heat and salt transport by eddies is proportional to $\Delta\rho$, while it is constant in their model (designated as M, which also includes the Ekman transport). This difference again makes the time-scale separation larger, but in this case, τ_T becomes smaller. The time scale τ_T is $(2\mu/\epsilon + \Delta\rho_s + \Delta T_s)^{-1}$, in which ΔT_s results from the variation in the eddy transport proportional to $\Delta\rho'$ in (8). Note that M in their theory roughly corresponds to $\Delta\rho_s$. As $2\mu/\epsilon$ and ΔT_s are positive, not only the boundary conditions in temperature and salinity but also the eddy transport characterized by the density gradient makes τ_T smaller than τ_S. It is worth noting that because of the variation in the eddy transport, precipitation changes $\Delta T'$ indirectly through $\Delta S'$ in (8). This point also makes the fourth difference from their results, as discussed in the next subsection.

The above three time scales determine the solution of (8) and (9). Thus, a relationship between the time scales and the solution of the DLEs gives physical insights into the DS and the dynamics of the idealized marginal sea. The DLEs are now examined separately for step function and sine function precipitation.

1) DLEs WITH STEP FUNCTION PRECIPITATION

The general solution for step function precipitation is obtained as follows,

$$\Delta T'(t) = \underbrace{\left[\Delta T'(t_0) - \frac{\Delta T_s \Delta S'(t_0)}{1/\tau_T - 1/\tau_S}\right] e^{-(t-t_0)/\tau_T} + \frac{\Delta T_s \Delta S'_h(t)}{1/\tau_T - 1/\tau_S}}_{\Delta T'_h(t)} + \Delta T'_p(t), \tag{10}$$

$$\Delta S'(t) = \underbrace{\Delta S'(t_0) e^{-(t-t_0)/\tau_S}}_{\Delta S'_h(t)} + \Delta S'_p(t), \tag{11}$$

$$\Delta T'_p(t) = \begin{cases} \dfrac{\tau_S \Delta\gamma' \Delta T_s}{4\epsilon}\left\{\tau_T[1 - e^{-(t-t_0)/\tau_T}] - \dfrac{1}{1/\tau_T - 1/\tau_S}[e^{-(t-t_0)/\tau_S} - e^{-(t-t_0)/\tau_T}]\right\} & (t<0) \\ \dfrac{\tau_S \Delta\gamma' \Delta T_s}{4\epsilon}\left[\tau_T(1 - e^{t_0/\tau_T})e^{-t/\tau_T} - \dfrac{e^{-t/\tau_T}}{1/\tau_T - 1/\tau_S}(e^{t_0/\tau_S} - e^{t_0/\tau_T}) + \dfrac{1 - e^{t_0/\tau_S}}{1/\tau_T - 1/\tau_S}(e^{-t/\tau_S} - e^{-t/\tau_T})\right] & (t \geq 0) \end{cases}, \quad \text{and} \tag{12}$$

$$\Delta S'_{\rm p}(t) = \begin{cases} \dfrac{\tau_S \Delta\gamma'}{4\epsilon}[1 - e^{-(t-t_0)/\tau_S}] & (t<0) \\ \dfrac{\tau_S \Delta\gamma'}{4\epsilon}(1 - e^{t_0/\tau_S})e^{-t/\tau_S} & (t \geq 0) \end{cases}, \quad (13)$$

where t_0 is the initial time, and subscripts h and p denote the homogeneous and particular solution, respectively. Here, t_0 is negative, meaning that the initial time is before $t = 0$ when precipitation changes instantaneously. When t_0 is positive or zero, $\Delta T'_{\rm p}(t) = \Delta S'_{\rm p}(t) = 0$, and the homogeneous solution remains only. It should be emphasized here that the general solution can satisfy any initial condition.

The general solution describes the relaxation toward the (steady) equilibrium state. When $t \geq 0$, the solution approaches zero, as $\Delta T_{\rm s}$ and $\Delta S_{\rm s}$ are the steady solution after the precipitation changes at $t = 0$. In contrast, when $t < 0$, $\Delta T'$ and $\Delta S'$ approaches $\tau_T \Delta T_{\rm s} \tau_S \Delta\gamma'/(4\epsilon)$ and $\tau_S \Delta\gamma'/(4\epsilon)$, respectively. Both values added to $\Delta T_{\rm s}$ and $\Delta S_{\rm s}$, respectively, are the approximate steady solution before the precipitation changes. When the precipitation strengthens at $t = 0$ (i.e., $\Delta\gamma' < 0$), the equilibrium values of ΔT and ΔS when $t \geq 0$ (i.e., $\Delta T_{\rm s}$ and $\Delta S_{\rm s}$) are larger than those in $t < 0$ [i.e., $\Delta T_{\rm s} + \tau_T \Delta T_{\rm s} \tau_S \Delta\gamma'/(4\epsilon)$ and $\Delta S_{\rm s} + \tau_S \Delta\gamma'/(4\epsilon)$, respectively]. This result means that the convective water in the interior becomes cold and fresh compared with that before the precipitation strengthens and is also consistent with the relation between the water mass properties and the magnitude of steady precipitation (Spall 2012).

The salinity relaxation is described by the exponential decay whose time scale is τ_S, while the temperature relaxation is dependent on the two different exponentials whose time scales are τ_S and τ_T, respectively. The values of τ_T and τ_S depend on $\Delta T_{\rm s}$ and/or $\Delta S_{\rm s}$, both of which are changed by $\Delta\gamma'$: 4.48 yr $< \tau_T^\star <$ 4.51 yr and 11.9 yr $< \tau_S^\star <$ 14.5 yr. In each case, τ_S is about 3 times as large as τ_T. Thus, the temperature relaxation is characterized not by the relaxation time scale of temperature τ_T but by that of salinity τ_S. This result essentially comes from the fact that temperature is indirectly changed by precipitation through the variation in the eddy transport represented by the term with $\Delta\rho'$ in (8). This point is the fourth difference from the theory by Wahlin and Johnson (2009). If the variation in the eddy transport is ignored as in Wahlin and Johnson (2009), the temperature relaxation is described by the exponential with the time scale τ_T.

Hereafter, the initial time t_0 is set to be zero, which makes the particular solution zero. It should be emphasized that the particular solution is similar to the homogeneous one as seen in (10)–(13); $\Delta T'_{\rm h}$ and $\Delta T'_{\rm p}$ consist of the exponentials characterized by τ_T or τ_S, while $\Delta S'_{\rm h}$ and $\Delta S'_{\rm p}$ are only by the exponential with the time scale τ_S. The treatments with $t_0 = 0$ make the comparisons with numerical simulations easier.

2) DLEs WITH SINE FUNCTION PRECIPITATION

The general solution for sine function precipitation is obtained as follows:

$$\Delta T'(t) = \frac{C}{\sqrt{1/\tau_S^2 + \omega^2}} \frac{\Delta T_{\rm s}}{\sqrt{1/\tau_T^2 + \omega^2}} \sin(\omega t - \phi_S - \phi_T) + T'_{\rm h}(t), \quad \text{and} \quad (14)$$

$$\Delta S'(t) = \frac{C}{\sqrt{1/\tau_S^2 + \omega^2}} \sin(\omega t - \phi_S) + S'_{\rm h}(t), \quad (15)$$

where $C \equiv -\Delta\gamma'/(4\epsilon)$, $\phi_T \equiv \tan^{-1}(\omega\tau_T)$, and $\phi_S \equiv \tan^{-1}(\omega\tau_S)$. Note again that the basic steady solution is the equilibrium without γ', where $-\gamma'(t)/(4\epsilon) = C\sin(\omega t)$. The first terms in (14) and (15) represent the particular solution with a sine function forcing, while the second ones are the homogenous solution whose forms are the same as those in (10) and (11). We further examine the particular solution in detail.

The phases (ϕ_T and ϕ_S) are determined only by the three time scales: $1/\omega$, τ_T, and τ_S, while the amplitudes of $\Delta T'$ and $\Delta S'$ depend on these time scales and are also linearly dependent on the precipitation amplitude through C. The value of $1/\omega$ should be used as the third time scale[1] rather than the precipitation period $2\pi/\omega$. This is because ω without 2π appears in the DS, DLEs, and their solutions. A magnitude relation between $1/\omega$, τ_T, and τ_S determines characteristics of the DLE solution. The value of $1/\omega$ is referred to as the period in this and the next subsection.

First, $\Delta S'$ is examined. When the forcing period is sufficiently long,[2] such that $1/\omega \gg \tau_S$, (9) is approximately reduced to $0 \approx -\Delta S'/\tau_S + C\sin(\omega t)$, indicating that the eddy salinity flux instantaneously balances the time-dependent precipitation. In other words, ΔS takes a quasi-steady state. The solution is also reduced to $\Delta S' \approx C\tau_S \sin(\omega t)$. When the precipitation is strong

[1] This treatment also has a mathematical reason. In general, a periodic solution has a form of $\sin(\omega t) = \sin(2\pi t/T_{\rm period})$, while an exponentially decaying solution is proportional to $\exp(-t/\tau_{\rm relax})$, where $T_{\rm period}$ and $\tau_{\rm relax}$ are positive constants. This difference in the solution suggests that ω (or $1/\omega$) should be compared with $1/\tau_{\rm relax}$ (or $\tau_{\rm relax}$).

[2] Note that we consider an asymptotic case here. Roughly speaking, the inequality means that $1/\omega$ is at least one order of magnitude larger than τ_S, while an asymptotic solution is sometimes valid outside the range of the inequality.

(i.e., $\sin(\omega t) \approx 1$), $\Delta S'$ is positive and large, which means that the interior is fresher than that with weak precipitation [i.e., when $\sin(\omega t)$ is negative]. The larger ΔS ($=\Delta S_s + \Delta S'$) generally means that the salinity of the interior S_I is lower, as ΔS is proportional to $S_{Bin} - S_I$, in which S_{Bin} is constant in the DS and nearly constant in the numerical model (the maximum variation is much smaller than 1% of the time-mean S_{Bin}). A similar thing is also observed for ΔT, but in this case, its large value indicates that the interior is cold.

On the other hand, when the forcing period is sufficiently short, such that $\tau_S \gg 1/\omega$, (9) is approximately reduced to $d\Delta S'/dt \approx C\sin(\omega t)$, which indicates that the adjustment due to the eddies is not effective. This is because the relaxation time scale by eddies τ_S is much longer than the precipitation period $1/\omega$. The solution is also reduced to $\Delta S' \approx -C/\omega\cos(\omega t)$. The maximum $\Delta S'$ lags 90° behind the γ' minimum, which means that the interior is freshest 90° after the strongest precipitation because freshwater accumulates in the interior. These are essentially one-dimensional solutions.

Similar discussion on $\Delta T'$ can be made; however, it is now the $\Delta S'$ variation that acts as a low-frequency forcing to $\Delta T'$. It should be emphasized again that precipitation changes $\Delta T'$ indirectly through the variation in $\Delta S'$ (i.e., variation in the eddy transport). More specifically, τ_S and $C\sin(\omega t)$ are replaced with τ_T and $\Delta T_s \Delta S'(t)$, respectively, in the previous discussion.

The DLE solution [(14) and (15)] indicates that the amplitudes of $\Delta T'$ and $\Delta S'$ tend to decrease with an increase in ω, and in particular $\Delta T'$ decreases more rapidly by a factor of $1/\sqrt{1/\tau_T^2 + \omega^2}$. This fact suggests that the marginal sea cannot follow the rapid (τ_T and $\tau_S \gg 1/\omega$) change in precipitation. It is also clear that the $\Delta T'$ amplitude is generally smaller than the $\Delta S'$ amplitude by a factor of $\Delta T_s/\sqrt{1/\tau_T^2 + \omega^2}$. This is because $\Delta S'$ is forced by precipitation, while $\Delta T'$ is forced by $\Delta S'$ whose amplitude is reduced by the eddy salinity fluxes.

c. *Temperature, salinity, and heat fluxes with sine function precipitation*

In this subsection, we examine the DS [(4) and (5)] with $\gamma' = \Delta\gamma'\sin(\omega t)$ and interpret results with the DLEs. Figures 3a and 3b show the time series of ΔT (solid curves), ΔS (dashed curves), and γ' (dashed–dotted curves) with 20- and 120-yr period, respectively, obtained from the DS after a sufficiently long time in which an influence of the initial adjustment described by the homogeneous solution in (14) and (15) is negligible. As predicted by the DLEs, the amplitudes of $\Delta T'$ and $\Delta S'$ increase with an increase in the period; the $\Delta T'$ amplitude is 4.8 times larger in Fig. 3b than in Fig. 3a, while that of $\Delta S'$ is 3.3 times larger. Note that the $\Delta T'$ amplitude is multiplied by 4 in Fig. 3a for ease of comparison, while such scaling is not used in Fig. 3b.

In the 20-yr periodic case (Fig. 3a), the responses of ΔT and ΔS to the precipitation are significantly delayed. This delay is supported by the time-scale separation: $\tau_T^\star = 4.5\,\text{yr}$ and $\tau_S^\star = 12.9\,\text{yr}$, while $1/\omega^\star = 20\,\text{yr}/(2\pi) \sim 3\,\text{yr}$. The magnitude relation is roughly categorized into the case with $\tau_S^\star$ and $\tau_T^\star > 1/\omega^\star$. Thus, the DLEs indicate that the ΔS maximum is about 90° behind the γ' minimum, while the ΔT maximum is about 90° behind the ΔS maximum, as seen in Fig. 3a, although the delay of the ΔT maximum is slightly overestimated by the DLEs. In contrast, Fig. 3b suggests that the 120-yr periodic solution is quasi steady at each time. The interior is coldest and freshest, that is, ΔT and ΔS are largest, when precipitation is strong, that is, $\gamma' < 0$. The time-scale separation also supports this quasi steadiness: as $1/\omega^\star = 120\,\text{yr}/(2\pi) \sim 20\,\text{yr}$, the magnitude relation is roughly categorized into the other case with $1/\omega^\star > \tau_S^\star$ and $\tau_T^\star$.

Next, the heat budget in the basin is analyzed by the meridional heat fluxes across the sill (referred to as HF_{sill}) and the heat fluxes across the sea surface (referred to as HF_{surf}). Precipitation indirectly causes variations of HF_{sill} and HF_{surf}. The term HF_{surf} is the sum of the heat fluxes across the surfaces of the interior and the boundary region as follows:

$$\begin{aligned} HF_{surf}^\star &= \Gamma[A(T_I - T_A) + PL(T_{Bin} - T_A)] \\ &= \frac{\rho_0 C_p A H_0 T^*}{\tau}\frac{2\mu}{\epsilon}(1 - \Delta T) + \Gamma T^* PL, \end{aligned} \quad (16)$$

where $HF_{surf}^\star$ is positive when heat is lost to the atmosphere (PL is the surface area of the boundary current). Here, the temperature change in the boundary current is ignored, as is consistent with assumption ii. Spall (2011) showed that, for similar configurations, the temperature change along the perimeter has to be taken into account by replacing P with an effective perimeter, when $\Gamma \geq 60\,\text{W m}^{-2}\,^\circ\text{C}^{-1}$. In the present paper, Γ is fixed to be $10\,\text{W m}^{-2}\,^\circ\text{C}^{-1}$, indicating that such treatment is not necessary.

The heat budget in the basin can be obtained by integrating the temperature equation over the basin:

$$\begin{aligned} \rho_0 C_p H_0 A \frac{dT_I}{dt^\star} = &\underbrace{\rho_0 C_p V H_{sill} L(T_{Bin} - T_{Bout})}_{HF_{sill}^\star} \\ &- \underbrace{\Gamma[A(T_I - T_A) + PL(T_{Bin} - T_A)]}_{HF_{surf}^\star}, \end{aligned} \quad (17)$$

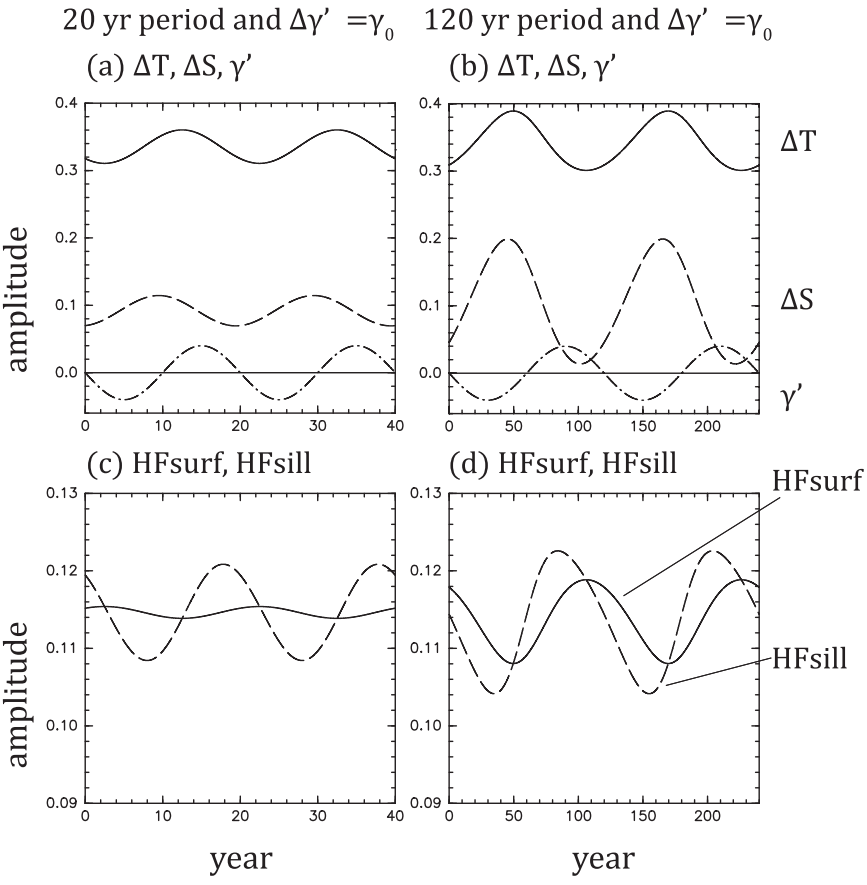

FIG. 3. Time series of ΔT (solid curves), ΔS (dashed curves), and $\gamma'(t)$ (dashed–dotted curves) for (a) 20- and (b) 120-yr periodic precipitation, all of which are obtained from the DS. (c),(d) As in (a) and (b), but for HF_{surf} (solid curves) and HF_{sill} (dashed curves). The $\gamma'(t)$ amplitude is equal to γ_0. The amplitude of $\Delta T'$ is multiplied by 4 in (a) and that of $\gamma'(t)$ is multiplied by 2.5 in (a) and (b) for ease of comparison.

where the temperature change in the boundary current is ignored again on the left-hand side. The term $HF^{\star}_{sill}$ is defined as the difference in heat fluxes between the east inflow and the west outflow (see Fig. 1), where $HF^{\star}_{sill}$ is positive when the net heat flows into the basin. The value $HF^{\star}_{sill}$ can be represented in terms of ΔT and ΔS by replacing the time derivative of T_I in (17) with the DS for ΔT [(4)]:

$$HF^{\star}_{sill} = \frac{\rho_0 C_p A H_0 T^*}{\tau} \Delta T |\Delta T - \Delta S| + \Gamma T^* P L. \quad (18)$$

The terms $HF^{\star}_{sill}$ and $HF^{\star}_{surf}$ are nondimensionalized by $\rho_0 C_p A H_0 T^*/\tau$. The value of HF_{sill} is equal to the sum of the eddy heat fluxes from the boundary current into the interior [the first term in (18)] and the heat fluxes across the sea surface in the boundary region [the second term in (18)]. In other words, some of the inflowing heat is lost to the atmosphere in the boundary current, some is carried into the interior via eddies, and the remainder exits the domain in the western outflow.

Both (16) and (18) are relevant regardless of the time dependency of precipitation, while generally $HF_{surf} \neq HF_{sill}$ as in (17) when precipitation is time dependent. A large difference between HF_{surf} and HF_{sill} results in heat storage in the interior.

Figures 3c and 3d show the time series of HF_{surf} (solid curves) and HF_{sill} (dashed curves) obtained from the DS during the same time intervals as those of Figs. 3a and 3b, respectively. The term HF_{surf} is out of phase with ΔT as is defined by (16), while the HF_{sill} phase is determined by that of eddy heat fluxes [the first term in (18)]. The DLEs indicate that the eddy heat flux term is characterized by $\Delta\rho$, that is, the strength of baroclinicity. This prediction is consistent with the fact that the phase difference of HF_{sill} from $\Delta\rho$ is between about -0.1 and -0.7 for the cases examined here, whose absolute values are one order of magnitude smaller than 2π (the maximum difference).

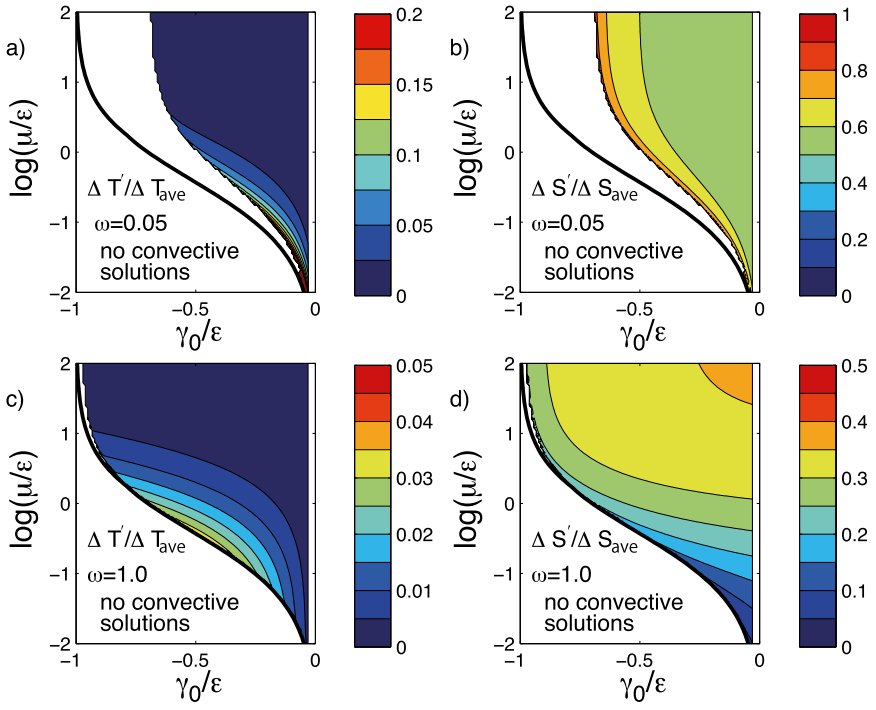

FIG. 4. Normalized amplitudes of $\Delta T'/\Delta T_{ave}$ and $\Delta S'/\Delta S_{ave}$ in the γ_0/ϵ–μ/ϵ space with (a),(b) $\omega = 0.05$ and (c),(d) $\omega = 1$, all of which are obtained from the DS with sine function precipitation [$\gamma'(t) = \Delta\gamma' \sin(\omega t)$]. Here, ΔT_{ave} and ΔS_{ave} are time-averaged values over one period, $\Delta T'$ and $\Delta S'$ are deviations from these averaged values, and $\Delta\gamma'$ is $\gamma_0/2$. White regions denote that a convective solution [i.e., $\Delta T(t) > 2\Delta S(t)$ for any t] does not exist, while thick black curves denote the boundaries of existence of steady thermal-mode solution (i.e., $\Delta T_s > 2\Delta S_s$) with $\Delta\gamma' = 0$.

The HF_{surf} amplitude significantly increases as the period is longer, while the HF_{sill} amplitude increases only slightly. The difference between HF_{sill} and HF_{surf} is proportional to the time derivative of T_I as in (17). Thus, Figs. 3c and 3d indicate that, when a period is short enough (i.e., $\tau_T, \tau_S \gg 1/\omega$), most of the fluctuations in the inflowing heat is used to change T_I rather than being lost to the atmosphere.

d. *Response to sine function precipitation with various γ_0 and μ*

We further examine the amplitudes of $\Delta T'$ and $\Delta S'$ obtained from the DS as functions of the controlling parameters. In this subsection, γ_0/ϵ and μ/ϵ are varied, while the frequency ω of the precipitation is fixed. Figure 4 shows normalized amplitudes of $\Delta T'/\Delta T_{ave}$ and $\Delta S'/\Delta S_{ave}$ with either $\omega = 0.05$ or $\omega = 1$, where ΔT_{ave} and ΔS_{ave} are time-averaged values over one period, and $\Delta T'$ and $\Delta S'$ are deviations from those averaged values, respectively. Here, $\Delta\gamma'$ is $\gamma_0/2$, which means that the precipitation amplitude varies as γ_0 is changed. White regions denote that a convective solution [or thermal-mode solution, i.e., $\Delta T(t) > 2\Delta S(t)$ for any t] does not exist. Thick black curves denote the boundaries of existence of steady thermal-mode solution with steady precipitation (see also Fig. 2 in Spall 2012). Note that $\Delta S_s = \Delta T_s/2$ on the thick black curves (Spall 2012).

The boundaries of colored regions do not match the thick black curves, which indicate hysteresis. Between the thick black curves and the boundaries of colored regions, steady thermal-mode solutions exist, while time-dependent ones do not. It is important to note that an increase in precipitation magnitude may change the thermal-mode state [i.e., $\Delta T(t) > 2\Delta S(t)$] into the haline-mode state [i.e., $\Delta S(t) > 0.5\Delta T(t)$]. The discordance between the thick black curves and the boundaries of colored regions means that a solution cannot get back to the thermal-mode state once it moves to the haline-mode state (i.e., hysteresis), even if the steady thermal-mode solution exists. Note that the time-dependent solution with $\Delta T(t) = 2\Delta S(t)$ does not exist for the DS [(4) and (5)]. The boundaries of the colored regions are closer to the thick black curves when $\omega = 1$. This is because the interior cannot strongly respond to a change in precipitation when the precipitation frequency is high enough (i.e., $\omega \gg 1/\tau_T, 1/\tau_S$), as discussed in section 2b.

In the low-frequency case (Figs. 4a,b), the state is always close to equilibrium. This means that the difference in the patterns of $\Delta T'/\Delta T_{\rm ave}$ and $\Delta S'/\Delta S_{\rm ave}$ can be understood by the DS with steady precipitation (Spall 2012); the amplitude of $\Delta S'$ increases as the precipitation magnitude ($|\gamma_0|/\epsilon$) is larger, while that of $\Delta T'$ is not strongly dependent on the precipitation except for near the thick black curve. The ratio $|\Delta T'/\Delta T_{\rm ave}|$ is generally much smaller than 1 except near the haline collapse.

In the high-frequency case (Figs. 4c,d), the pattern of $\Delta T'/\Delta T_{\rm ave}$ is similar to the low-frequency pattern, while that of $\Delta S'/\Delta S_{\rm ave}$ is different. The DLEs are considered to be valid when $\omega = 1$ because the normalized amplitudes of deviations are small. In fact, the patterns (Figs. 4c,d) are quite similar to those obtained by the DLEs (not shown). Thus, the physical nature of the patterns can be understood by the DLE solution.

The amplitudes of the DLE solution [i.e., the particular solution in (14) and (15)] can be further approximated in the following when $\omega^2(=1) \gg 1/\tau_S^2$ and $1/\tau_T \approx 2\mu/\epsilon$:

$$\text{Amplitude of } \frac{\Delta T'}{\Delta T_{\rm s}} \approx \frac{C}{\sqrt{1/\tau_S^2+\omega^2}\sqrt{1/\tau_T^2+\omega^2}} \sim \frac{|\gamma_0|/\epsilon}{8\sqrt{(2\mu/\epsilon)^2+1}}, \quad \text{and} \tag{19}$$

$$\text{Amplitude of } \frac{\Delta S'}{\Delta S_{\rm s}} \approx \frac{C}{\Delta S_{\rm s}\sqrt{1/\tau_S^2+\omega^2}} \sim \frac{|\gamma_0|/\epsilon}{8\Delta S_{\rm s}}, \tag{20}$$

where $C \equiv -\Delta\gamma'/(4\epsilon)$ is equal to $|\gamma_0|/(8\epsilon)$ under the present setting. Note that $\Delta T_{\rm ave} = \Delta T_{\rm s}$ and $\Delta S_{\rm ave} = \Delta S_{\rm s}$ for the DLE solution. The amplitude of $\Delta T'/\Delta T_{\rm s}$ is larger as the precipitation amplitude ($\propto|\gamma_0|$) is larger and/or the thermal relaxation characterized by $2\mu/\epsilon$ is weaker, as seen in Fig. 4c. The amplitude of $\Delta S'/\Delta S_{\rm s}$ does not vary much with changes in $|\gamma_0|/\epsilon$ when this parameter is small as seen in Fig. 4d, because in this case $\Delta S_{\rm s}$ is roughly proportional to $|\gamma_0|/\epsilon$. In contrast, the amplitude of $\Delta S'/\Delta S_{\rm s}$ is smaller when the parameters are close to the thick black curve because $\Delta S_{\rm s}$ increases rapidly near there (see Fig. 2b in Spall 2012). The similar feature is seen in Fig. 4d.

These results clarify that the pattern difference between Figs. 4b and 4d is due to the difference in the strength of the response to precipitation. When the frequency is low, $\Delta S'$ has larger amplitude (i.e., the response to precipitation is strong) and $|\gamma_0|$ determines the pattern as in Fig. 4b. In contrast, $\Delta S'$ with high-frequency forcing has smaller amplitude (i.e., the response to precipitation is weak), and the pattern of Fig. 4d is determined not by $\Delta S'(\propto|\gamma_0|)$ but by $|\gamma_0|/\Delta S_{\rm s}$.

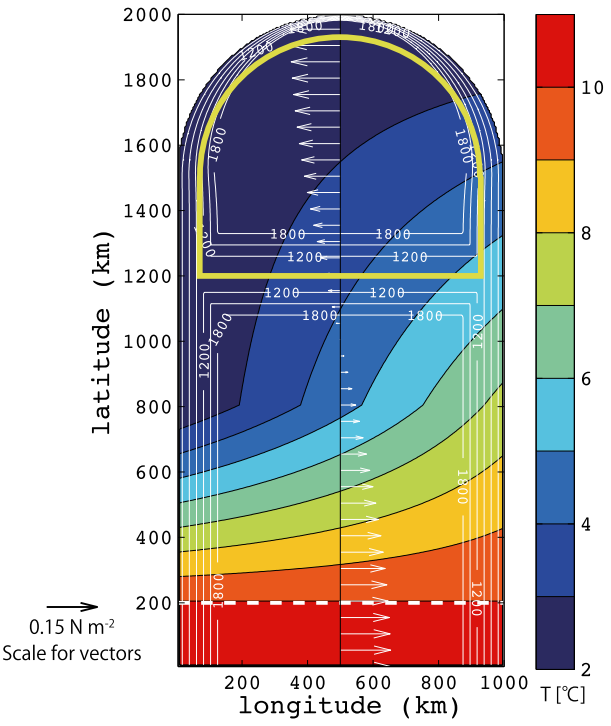

FIG. 5. Model domain, bottom topography (white contours; CI = 300 m), wind stress (vectors, independent of longitudes), and atmospheric temperature toward which the model sea surface temperature is restored (colors). Temperature is restored toward a uniform stratification, and salinity is restored toward 35 ppt in the region south of the bold dashed white line at 200 km latitude. Precipitation is nonzero over the entire region north of the sill at 1200-km latitude. The region enclosed by the thick yellow curve is the region over which temperature and salinity are respectively averaged to obtain $T_{\rm I}$ and $S_{\rm I}$.

3. Comparisons with an eddy-resolving numerical model

a. *Model configuration*

The DS has given the inherent time scales and the evolution of temperature and salinity as well as aided in the physical interpretation of the ocean response to changes in precipitation. However, it is not clear whether the DS prediction is valid because the DS is a greatly simplified system using assumptions i–iv, and these assumptions may not be well satisfied in a more realistic model or the real ocean. Thus, it is desirable to evaluate the basic predictions of the DS. In this section, following Spall (2012), an eddy-resolving ocean circulation model is configured in an idealized basin that is subject to wind stress and heat and freshwater flux forcing. Note that wind stress is included in the numerical model, while it is not in the DS. An advantage of the idealized configuration is that nondimensional parameters such as μ, ϵ, and γ_0 are easily obtained, which makes

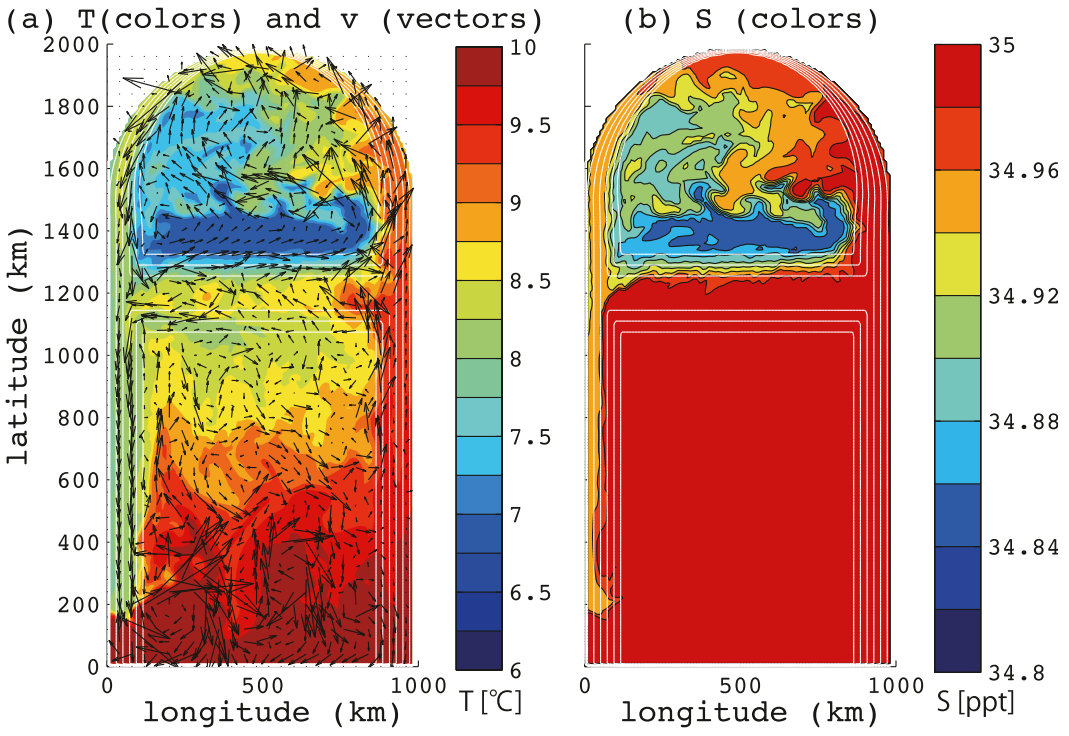

FIG. 6. The initial state obtained after the 24-yr spinup: (a) sea surface temperature (colors) and horizontal velocity (vectors; every fourth grid point) and (b) sea surface salinity (colors). White contours are the bottom topography, with CI of 300 m.

it easy to compare results to the DS predictions. If there is a good agreement between them, the physical understanding obtained from the DS can be applied to the more complex general circulation model that includes such things as resolved mesoscale eddies, wind forcing, and a barotropic mode.

The numerical model is the Massachusetts Institute of Technology general circulation model (MITgcm; Marshall et al. 1997). The model configuration is almost the same as in Spall (2012) except for the addition of a prescribed time-dependent precipitation north of 1200-km latitude (either a step function or a sine function in time). Figure 5 shows the model domain with atmospheric temperature (colors) and wind stress (vectors, independent of longitude). The model domain can be divided into three regions: north of the sill at 1200-km latitude is the idealized marginal sea; the region between 1200- and 200-km latitudes is regard as a subpolar gyre; and south of 200-km latitude is regarded as the rest of the World Ocean (Spall 2011).

For all calculations, the sill depth is 1000 m, the atmospheric restoring strength Γ is $10\,\mathrm{W\,m^{-2}\,°C^{-1}}$, and the basic precipitation $E_0 = -2 \times 10^{-8}\,\mathrm{m\,s^{-1}}$ north of 1200-km latitude. Sensitivity of the mean state to each of these parameters is discussed by Spall (2012). The model is started at a state of rest with an initial stratification of $N^2 = 2 \times 10^{-6}\,\mathrm{s^{-2}}$ and upper-level temperature of 10°C. Note that the initial stratification does not affect the statistically steady state, and the upper-level temperature of 10°C provides T^* that is roughly consistent with that in the Nordic and Labrador Seas (Spall 2004, 2011, 2012). The model is run for a period of 24 yr, which is sufficient to approach a statistically steady state (as indicated by basin-integrated available potential energy or kinetic energy and also diagnosed quantities such as ΔT and ΔS). After the 24-yr spinup, the time-dependent precipitation is added to the north of 1200-km latitude.

Figure 6 shows temperature, horizontal velocity, and salinity at the sea surface at the end of year 24 (i.e., the initial state). The cyclonic boundary current is observed along the bottom topography; it flows northward along the eastern boundary at low latitudes, crosses the sill at the 1200-km latitude and continues flowing northward along the eastern boundary. It is also found that eddies are shed off from the boundary current. The temperature in the boundary current decreases along the boundary pathway as a result of heat loss to the atmosphere and eddy fluxes into the interior. The salinity also decreases along the boundary due to precipitation and eddy fluxes. The coldest and freshest waters are found in the interior region: $T \approx 6.8$°C and $S \approx 34.8$ ppt. The water flowing southward along the western boundary

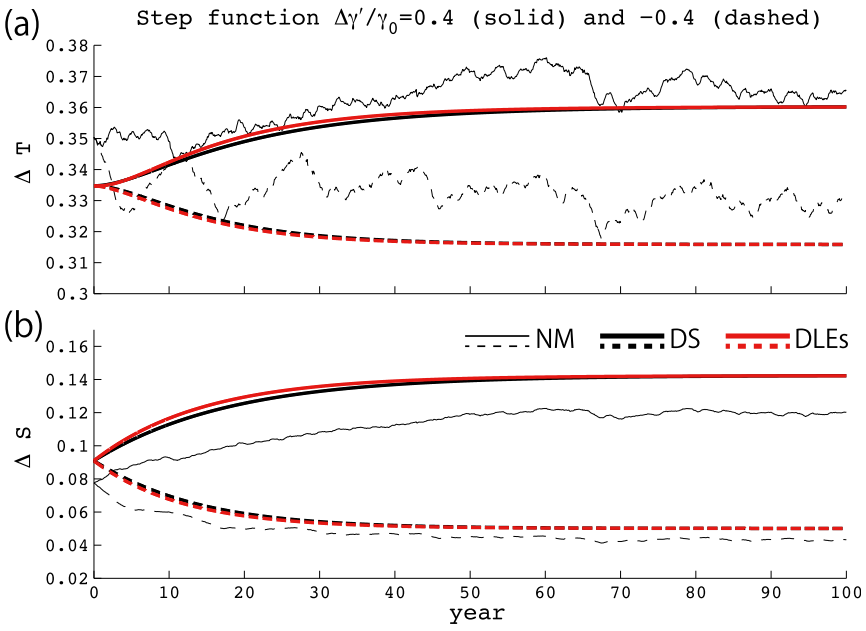

FIG. 7. (a) Time series of ΔT obtained from the NM (thin curves), DS (thick black curves), and DLEs (thick red curves) with the step function precipitation. (b) As in (a), but for ΔS. In each figure, solid curves are for $\Delta\gamma'/\gamma_0 = 0.4$ (strong precipitation), while dashed ones are for $\Delta\gamma'/\gamma_0 = -0.4$ (weak precipitation).

($T_{\mathrm{Bout}} = 8.0°\mathrm{C}$ and $S_{\mathrm{Bout}} = 34.9$ ppt) is colder and fresher than the northward-flowing water along the eastern boundary ($T_{\mathrm{Bin}} = 9.3°\mathrm{C}$ and $S_{\mathrm{Bin}} = 35.0$ ppt). The dynamics of the boundary current observed here is examined theoretically by Wahlin and Johnson (2009). These basic features are consistent with the observed circulation in the northern North Atlantic Ocean and Nordic Seas (Spall 2011, 2012) and are observed even for the strongest precipitation in the present paper (i.e., $\gamma' = \Delta\gamma' \sin(\omega^\star t^\star)$ with $\Delta\gamma' = \gamma_0$ and $\omega^\star = 2\pi/120$ yr).

b. Step function precipitation

We first consider cases with step function in precipitation. As in the DS, $\Delta T \equiv (T_{\mathrm{Bin}} - T_{\mathrm{I}})/T^*$ and $\Delta S \equiv (S_{\mathrm{Bin}} - S_{\mathrm{I}})\alpha_S/(\alpha_T T^*)$, where $T^* = 6.2°\mathrm{C}$, $\alpha_S = 0.8\,\mathrm{kg\,m^{-3}\,°C^{-1}}$ and $\alpha_T = 0.2\,\mathrm{kg\,m^{-3}\,°C^{-1}}$. Values of T_{I} and S_{I} are the instantaneous temperature and salinity spatially averaged over the region enclosed by the thick yellow curve in Fig. 5 and down to the bottom, respectively. Eastern and western parts of the curve are located on the isobath with the sill depth, while its northern part is not on the isobath to avoid containing the boundary current near there. It is confirmed that the following results are not overly sensitive to the choice of the yellow curve in Fig. 5. The values of T_{Bin} and S_{Bin} are transport weighted inflowing temperature and salinity along the eastern boundary at the 1200-km latitude, respectively. Here, we use their initial values to obtain ΔT and ΔS, as their standard deviations are smaller than 1% of the respective time-mean values due to the restoring in the southern region. The above definitions of ΔT and ΔS from the numerical model data correspond to those in the DS theory.

The model is run further for 100 yr with the additional constant precipitation E' north of 1200-km latitude whose magnitude is either ± 0.4, ± 0.3, ± 0.2, or $\pm 0.1 \times E_0$ (i.e., nondimensional magnitude $\Delta\gamma'$ of the step function is either ± 0.4, ± 0.3, ± 0.2, or $\pm 0.1 \times \gamma_0$). Figure 7 shows the time series of ΔT and ΔS with $\Delta\gamma'/\gamma_0 = 0.4$ (solid curves and strong precipitation) and $\Delta\gamma'/\gamma_0 = -0.4$ (dashed curves, weak precipitation) as typical examples. The DLEs give almost the same time series as those from the DS. The DS and DLEs predict the transitions to the new statistical equilibrium states reasonably well, aside from small initial offsets that reflect errors in the steady theory.

Significant variability on 5–10-yr time scales is observed in the time series of ΔT, while ΔS has similar fluctuation with about one-third magnitude (Fig. 7). The forcings are constant in time except for the initial step function precipitation. This fact suggests that these fluctuations are the natural variability inherent to the eddy-resolving numerical model rather than the forced variability. The DS with steady precipitation gives a constant solution, which means that such variability is not included in the DS theory. Physically, this is likely

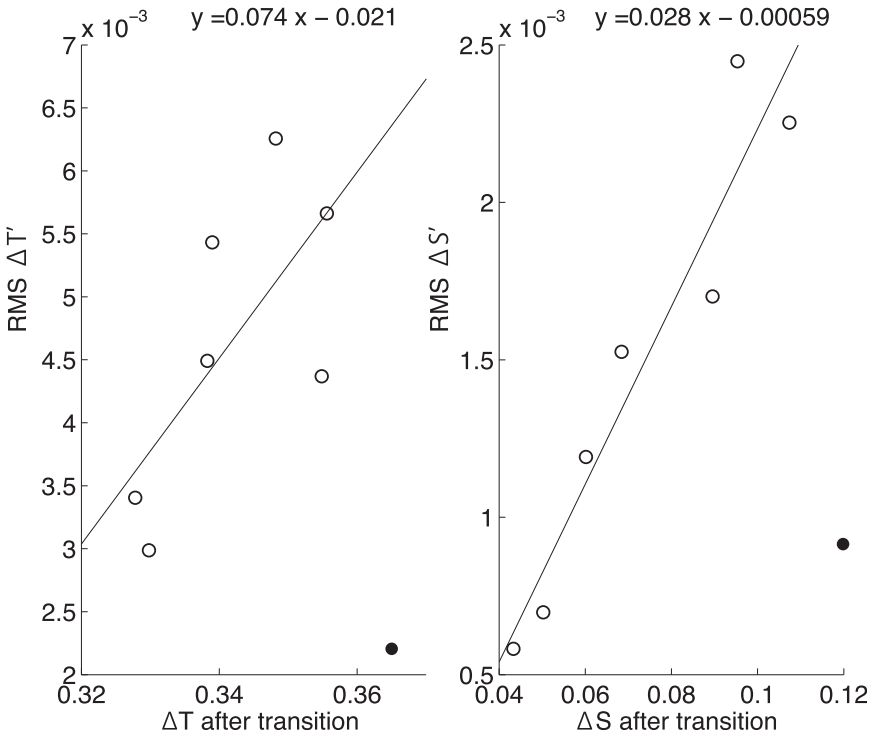

FIG. 8. (a) Scatterplot of RMS values of ΔT variation against ΔT_{AT}, which is the ΔT averaged over the last 20 yr for step function precipitation. (b) As in (a), but for ΔS. The line in each figure is obtained by the least squares fitting for open circles, whose equation is shown in the upper part.

because the parameterization of eddy fluxes is not complete, and an influence due to the spatial variation in the eddy field is not taken into account in the DS.

Small variations in the number of eddies formed or present in the interior will change the spatially averaged values of temperature and salinity (i.e., ΔT and ΔS). It is expected that if the fluctuation results from the variation in the number of eddies present in the interior, the magnitude of the variation can be approximately estimated by the time-mean value of ΔT or ΔS. This is because the temperature and salinity transported by eddies can be estimated by the differences in temperature and salinity at the origin of eddies, respectively (e.g., Visbeck et al. 1996; Spall and Chapman 1998). Time-mean values of ΔT and ΔS over the last 20 yr are used as the equilibrium values after transition and designated as ΔT_{AT} and ΔS_{AT}, respectively. Root-mean-square (RMS) values of variations in ΔT and ΔS over the last 20 yr are plotted against ΔT_{AT} and ΔS_{AT} in Figs. 8a and 8b, respectively. The RMS values of temperature are about 3 times as large as those of salinity. This is reflected by the large fluctuation in ΔT (Fig. 7). The line, obtained by the least squares fit, gives the rough estimate of fluctuation magnitude as a function of either ΔT_{AT} or ΔS_{AT}. The fluctuation tends to be large as the mean value is larger, consistent with the idea that it represents random variation in the amount of boundary current water in the interior. The closed circle with $\Delta\gamma' = 0.4\gamma_0$ is excluded to obtain the line in each figure. The large difference of the closed circle from the line may be attributed to the weakest baroclinicity with the smallest $\Delta\rho$ (=0.24), that is, the weakest eddy activity.

To simultaneously compare all the results, a transition time is introduced as the minimum time such that $|\Delta S(t) - \Delta S_{AT}|/\Delta S(0) < 0.1$. Figures 9a–d show transition time, ΔT_{AT}, ΔS_{AT}, and $\Delta\rho_{AT}$, respectively, where $\Delta\rho_{AT} \equiv \Delta T_{AT} - \Delta S_{AT}$. Note that precipitation strengthens at the initial time when $\Delta\gamma'/\gamma_0 > 0$. The solid curves are obtained from the DS, while the dashed ones in Fig. 9a are from the DLEs. The DLEs give a reasonably good estimate of transition time, although it is somewhat underestimated compared with the value from the DS. The DLEs give the same ΔT_{AT} and ΔS_{AT} as those from the DS because the basic steady state of the DLEs is the equilibrium after transition.

The DS predicts the results from the numerical model well, in particular, the asymmetry of transition time around

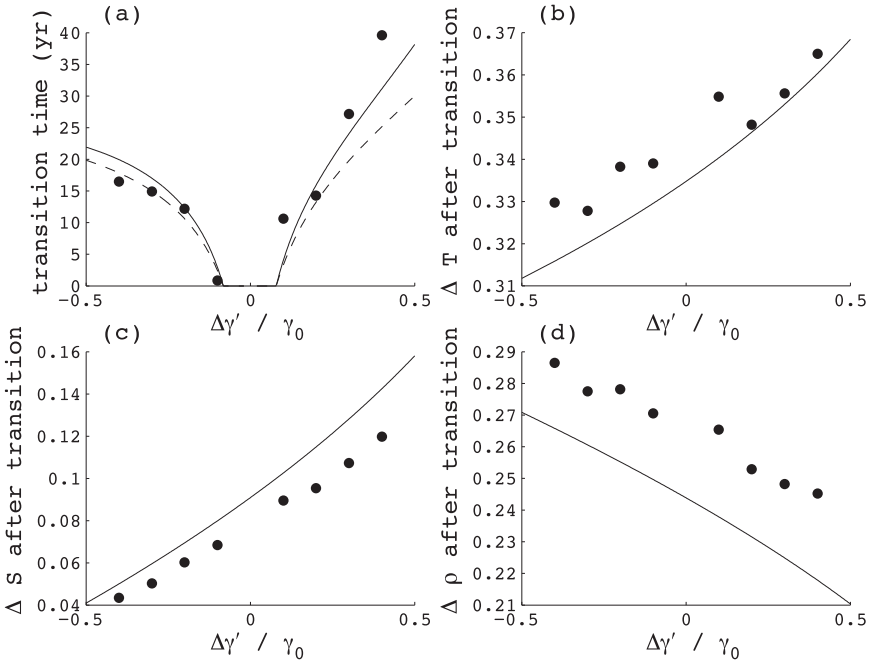

FIG. 9. Scatterplots of (a) transition time, (b) ΔT, (c) ΔS, and (d) $\Delta\rho$ against the normalized magnitude $\Delta\gamma'/\gamma_0$ of the step function precipitation, all of which are obtained from the numerical model. All solid curves are obtained from the DS, while dashed ones in (a) are from the DLEs. The terms ΔT, ΔS, and $\Delta\rho$ are the values averaged over the last 20 yr.

$\Delta\gamma'/\gamma_0$ (Fig. 9a). Figures 9b–d indicate that the convective water in the interior tends to be cold, fresh, and light, as precipitation is stronger (i.e., $\Delta\gamma'/\Delta\gamma_0$ is larger). This result is consistent with the DS theory and numerical simulations with steady precipitation (Spall 2012). There are small offsets in the magnitudes of ΔT, ΔS, and $\Delta\rho$ resulting from errors in the steady theory, although our primary interest here is the general dependence of these quantities on the parameter $\Delta\gamma'/\gamma_0$.

The DLE [(9)] and its solution [(11)] suggest that the transition time is characterized by the eddy flushing time scale τ_S. As predicted from the DS with steady precipitation (Spall 2012), $\Delta\rho_s$ is small when precipitation is strong, meaning that τ_S ($=1/\Delta\rho_s$) is large. Physically, the transition is made by eddy fluxes, which are roughly proportional to the density gradient between the interior and the boundary current. When $\Delta\gamma'/\gamma_0 > 0$, that is, precipitation strengthens at the initial time, eddy fluxes become weaker and it takes more time to make a transition, as seen in Fig. 9a. Figure 9d shows that $\Delta\rho$ after the transition actually tends to be small as $\Delta\gamma'/\gamma_0$ is larger.

c. *Sine function precipitation*

Cases with sine function precipitation are examined in this subsection. The model is run further for two periods with precipitation $E' = \Delta E' \sin(\omega^\star t^\star)$ north of 1200-km latitude. Amplitudes and periods used in the present paper are shown in Table 2, in which nondimensional numbers $\Delta\gamma'$ and γ_0 correspond to $\Delta E'$ and E_0, respectively. Simulations with doubled horizontal resolution are also performed (runs 19–27) to validate the lower-resolution results.

Figure 10 shows the time series of ΔT, ΔS, and γ' for 20- and 120-yr periodic precipitation whose amplitudes are γ_0 as typical examples. The time series from the DS and the DLEs include the initial adjustments, unlike Fig. 3, which are well described by the DLE general solutions (14) and (15). The DLEs give almost the same time series as those from the DS for the 20-yr periodic precipitation (Fig. 10a). Even in the 120-yr period case (Fig. 10b), the DLEs give similar curves, although the maxima are underestimated. This underestimation is likely attributed to an overestimation of $\Delta\rho'$ due to the lack of nonlinearity in the DLEs. This overestimated $\Delta\rho'$ makes the eddy flux terms larger, which reduce $\Delta T'$ and $\Delta S'$. The amplitude of eddy heat fluxes is actually overestimated by the DLEs as discussed in the next subsection, while similar overestimation is observed in the eddy salinity fluxes (not shown).

Next, we compare the time series from the DS with those from the numerical model. The DS predicts ΔS for the 20- and 120-yr periodic precipitation well (Figs. 10a,b), although the amplitudes are overestimated. The term ΔT is also predicted well in the 120-yr period

TABLE 2. Summary of model runs with sine function precipitation. The ratio of sine function amplitude to the constant precipitation is designated as $\Delta\gamma'/\gamma_0$ using nondimensional numbers. The color indicated in the far-right column is the one used in the scatterplots (Figs. 11, 13).

Run	$\Delta\gamma'/\gamma_0$	Period (yr)	Horizontal resolution (km)	Color
1	1/8	10	10	Gray
2	1/8	20	10	Gray
3	1/8	40	10	Gray
4	1/8	60	10	Gray
5	1/8	80	10	Gray
6	1/8	120	10	Gray
7	1/2	10	10	Red
8	1/2	20	10	Red
9	1/2	40	10	Red
10	1/2	60	10	Red
11	1/2	80	10	Red
12	1/2	120	10	Red
13	1	10	10	Black
14	1	20	10	Black
15	1	40	10	Black
16	1	60	10	Black
17	1	80	10	Black
18	1	120	10	Black
19	1/8	80	5	Magenta
20	1/2	10	5	Blue
21	1/2	20	5	Blue
22	1/2	80	5	Blue
23	1	10	5	Green
24	1	20	5	Green
25	1	80	5	Green
26	−0.5	10	5	Cyan
27	−0.5	20	5	Cyan

case (Fig. 10b), although the amplitude is again overestimated, and the phase is slightly different. The overestimation of amplitude by the DS may be attributed to errors in $\Delta\rho$, which are affected by the vertical stratification in the model, while the vertically uniform structure of the interior is assumed in the DS theory (assumption iv). The DS fails to describe the time series of ΔT with the 20-yr periodic precipitation (Fig. 10a). The 20-yr periodic component is not dominant in ΔT from the numerical model, and the time series are sensitive to the model resolution. Similar results are obtained for ΔT in most cases with 10- or 20-yr periodic precipitation. This is likely because the amplitude of the oscillation forced by the precipitation is smaller than the natural variability inherent in the numerical model, as discussed in section 3b. The magnitudes of natural variability can be estimated by the lines in Fig. 8. In the 20-yr period case, the magnitude of fluctuation in ΔT is the same order of magnitude as the predicted amplitude of $\Delta T'$ by the DS, while for ΔS the magnitude of fluctuation is an order of magnitude less.

These basic behaviors of ΔT and ΔS are also found for longer model runs (not shown) and for runs with doubled resolution. The term ΔT from the numerical model with 10- or 20-yr periodic precipitation is not analyzed further because the signal predicted by the DS is not larger than the inherent variability in the model. On the other hand, ΔS has weak inherent fluctuation and is analyzed for all cases.

To evaluate the basic parameter dependency predicted by the DS, the amplitude and phase of ΔT are obtained after detrending and filtering out high-frequency components: ΔT amplitude is the difference between max ΔT and min ΔT divided by 2, and its phase is the time, when ΔT first takes a local maximum, divided by the precipitation period. The amplitude and phase of ΔS are also obtained in the same way. Figure 11 shows the comparisons in amplitude and phase between the numerical model (NM) and the DS. The ratios of the values by the DS to the ones by the model are between 0.9 and 1.8 in Figs. 11b and 11d and between 0.5 and 2.5 in Figs. 11a and 11c except for the closed gray circle (ratio is 3.9) in Fig. 11c, which is excluded to obtain the line by least squares fit because of the exceptionally large ratio. Although the line slopes are not equal to one, they are $O(1)$, which provides general support for the scaling approach taken here. A few gray circles, including the closed one, with $\Delta\gamma'/\gamma_0 = 1/8$ (i.e., the smallest amplitude of precipitation) are not close to the lines in Figs. 11c and 11d. This is likely due to the small amplitude of the forced component and the relatively large background fluctuation.

The ΔT and ΔS amplitudes tend to be large as the precipitation period or amplitude is larger (Figs. 11a,b). This result is consistent with the prediction in sections 2b and 2c that the response to changes in precipitation is stronger as the precipitation period or amplitude is larger. The ΔT and ΔS phases tend to be small as the precipitation period is longer, while they are not strongly dependent on the precipitation amplitude (Figs. 11c,d). This result is also consistent with the prediction in sections 2b and 2c that the interior approaches a quasi-steady state as the precipitation period is longer, in which the interior is the freshest and coldest when precipitation is the strongest, while the response of the interior lags as the precipitation period is shorter.

It is worthwhile to compare the results with those from observational studies. The real ocean is affected by variability in the atmosphere through heat and freshwater fluxes and wind stress. It may be difficult to distinguish signals forced only by freshwater fluxes from observational data. The DS theory suggests that the relaxation time scales for temperature and salinity are determined by the time-mean state and are not largely affected by variability in the atmosphere. Thus, we

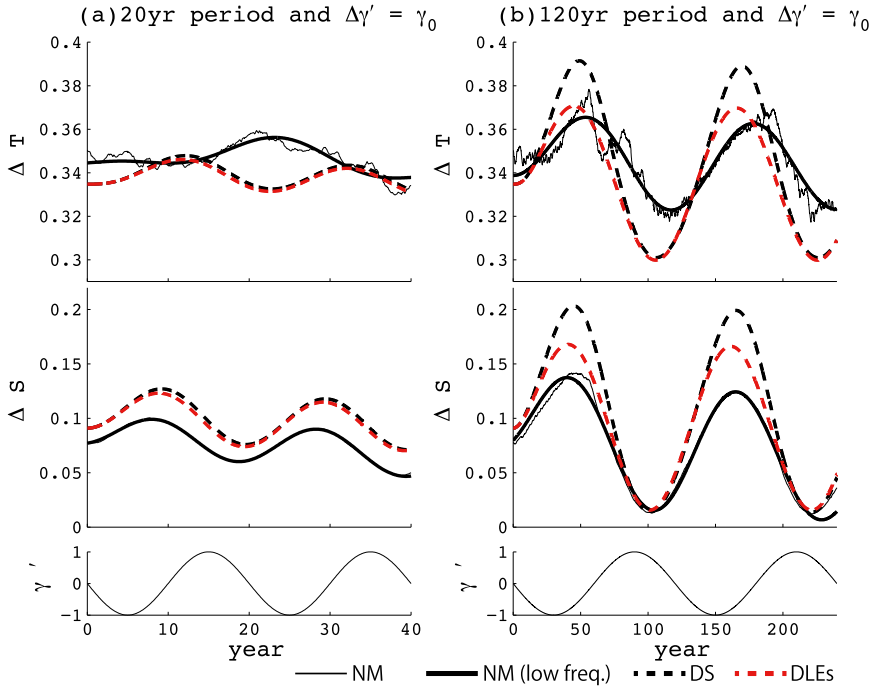

FIG. 10. (a) Time series of (top) ΔT, (middle) ΔS, and (bottom) γ' for the 20-yr periodic precipitation whose nondimensionalized amplitude is γ_0. Thin solid curves are obtained from the NM and thick solid ones are their low-frequency components. Black dashed curves are obtained from the DS, while red ones are from the DLEs. The γ' amplitude is normalized to unity. (b) As in (a), but for the 120-yr periodic precipitation.

compare the relaxation time scales with those suggested by observational studies. Van Aken et al. (2011) compared the time series of temperature (and potential temperature) at intermediate depths in the central Labrador Sea from the hydrographic data with those of surface heat fluxes estimated from the NCEP–NCAR reanalysis data between 1950 and 2010 (see Figs. 5 and 11 in their paper). They argued that the lowest temperature in the 50-yr harmonic fit lags 6 yr behind the maximum of heat fluxes. This time scale is between the two relaxation time scales τ_T [$=O(5)$ yr] and τ_S [$=O(10)$ yr], suggesting that our theoretical prediction on time scales is consistent with their results.

Observations in the Labrador Sea during the period of 1969 to 1972 may also be appropriate for the comparison here because anomalous freshwater input was considered to have caused a shutdown of deep convection. Straneo (2006) showed a good agreement between the time series of dense-layer thickness from her theory and that from the data at the Ocean Weather Station Bravo during that period. Her theory indicates that the flushing time scale, which is the same as τ_S, is the time scale for dense-layer thickness. This suggests that τ_S is a relevant time scale of ocean response to changes in precipitation.

The results from the numerical model with both step function and sine function precipitation support the qualitative validity of the DS. Thus, it is possible to use the DS to derive a basic understanding of the physics that controls the ocean response to changes in precipitation and its dependence on parameters such as precipitation magnitude and period.

d. *Heat fluxes with sine function precipitation*

The terms HF_{surf} and HF_{sill} are compared when precipitation is a sine function, and the physical understanding of the heat budget obtained from the DS is tested. Figure 12 shows the time series of HF_{surf}, HF_{sill}, and γ' obtained from the DS, DLEs, and numerical model for the 20- and 120-yr periodic precipitation. The DLEs give almost the same time series as those from the DS for the 20-yr periodic precipitation (Fig. 12a). In contrast, in the 120-yr period case (Fig. 12b), the minima of HF_{surf} and HF_{sill} are larger in the DLEs than in the DS. This result means that the eddy heat flux term [the first term in (18)] is overestimated by the DLEs. This overestimation is reflected in the underestimation of $\Delta T'$ by the DLEs compared with that by the DS (Fig. 10b).

Next, we compare the time series from the DS with those from the numerical model. In the 20-yr period case (Fig. 12a), the DS fails to predict the time series by the numerical model, since the 20-yr periodic component is not dominant in HF_{surf} and HF_{sill} from the model. The

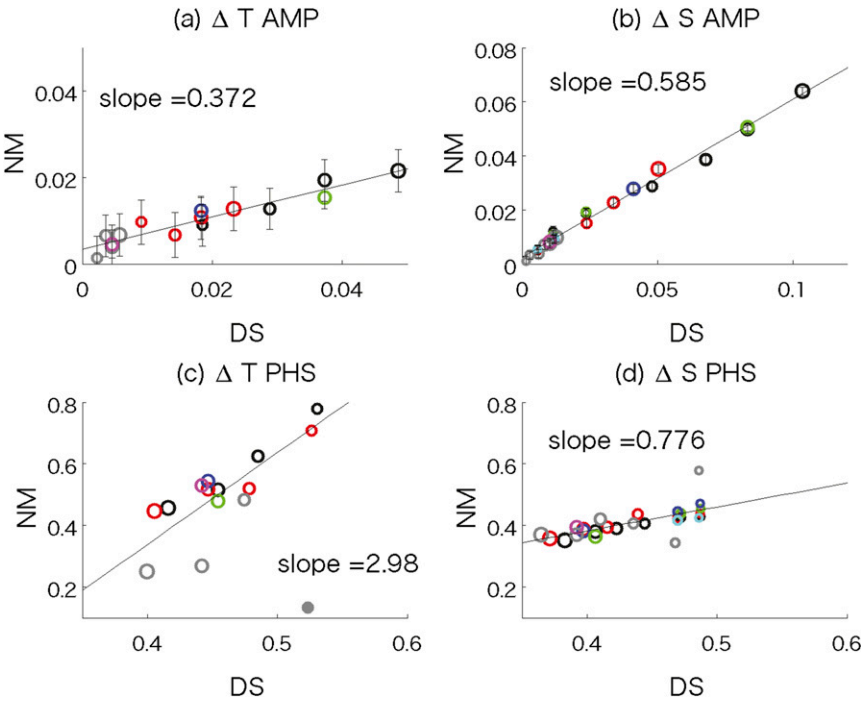

FIG. 11. Comparisons of (a) ΔT amplitude, (b) ΔS amplitude, (c) ΔT phase, and (d) ΔS phase from the NM with those from the DS for sine function precipitation. A circle in each figure is larger as a precipitation period is longer. Colors used in each figure are denoted in Table 2. The line in each figure is obtained by the least squares fitting. A closed gray circle in (c) is excluded to obtain the line. A value for the 10- or 20-yr periodic precipitation is not shown in (a) and (c). Error bars in (a) and (b) are obtained by substituting the mean values of ΔT and ΔS into the equations of the lines in Figs. 8a and 8b, respectively. Here, the mean value is the sum of the time-averaged value and the amplitude of oscillation multiplied by $1/\sqrt{2}$. Note that the axis ranges in (c) are the same as in (d).

fluctuation in HF_{surf} is likely due to the inherent variability in the model that was discussed in sections 3b and 3c. On the other hand, individual warm and cold water events crossing the sill likely make the strong high-frequency fluctuation in HF_{sill}. These events include large-scale meanders or bursts of anomalous water from the boundary current near the sill, which are not taken into account in the DS theory. In the 120-yr periodic case (Fig. 12b), the time series of HF_{surf} and HF_{sill} from the DS get closer to those from the numerical model, although there are still discrepancies between them.

As for ΔT, the internal fluctuations of HF_{surf} and HF_{sill} are dominant over the oscillations forced by precipitation with the 10- or 20-yr period, and the time series from the numerical model depend on the resolution. This suggests that small-scale motions are important for these short-periodic cases, which are not taken into account in the DS. Thus, it is beyond the scope of this paper to examine the short-periodic (10 or 20 yr) cases. In addition, Gulev et al. (2013) argued on the basis of the analyses of the observational data that short time scale ($\leq$10 yr) components of surface heat flux over the North Atlantic Ocean are mainly controlled by the atmosphere, which are highly fluctuated, while the longer ones are by the ocean. Thus, it is suggested that the short-periodic (10 or 20 yr) components shown above will be modified more strongly than long-periodic ones by the atmospheric variability in a coupled ocean–atmosphere system.

Figure 13 shows the amplitudes and phases of HF_{surf} and HF_{sill} obtained as those of ΔT and ΔS. The DS predicts the qualitative parameter dependences in the numerical model and once again the line slopes are $O(1)$. The scatterplots of HF_{surf} amplitude and phase (Figs. 13a,c) are similar to those of ΔT amplitude and phase (Figs. 11a,c), respectively. This is likely because HFsurf is determined by the sea surface temperature in the numerical model, while it is given by ΔT in the DS as seen in (16). The DS does not well predict the tendency of HF_{sill} amplitudes in the model (Fig. 13b), especially when precipitation is the strongest ($\Delta\gamma' = \gamma_0$, denoted by the black circles); the HF_{sill} amplitude in the model tends to be large as the precipitation period is longer, unlike for that in the DS. This is possibly due to the strong high-frequency fluctuation in HF_{sill} (Fig. 12b).

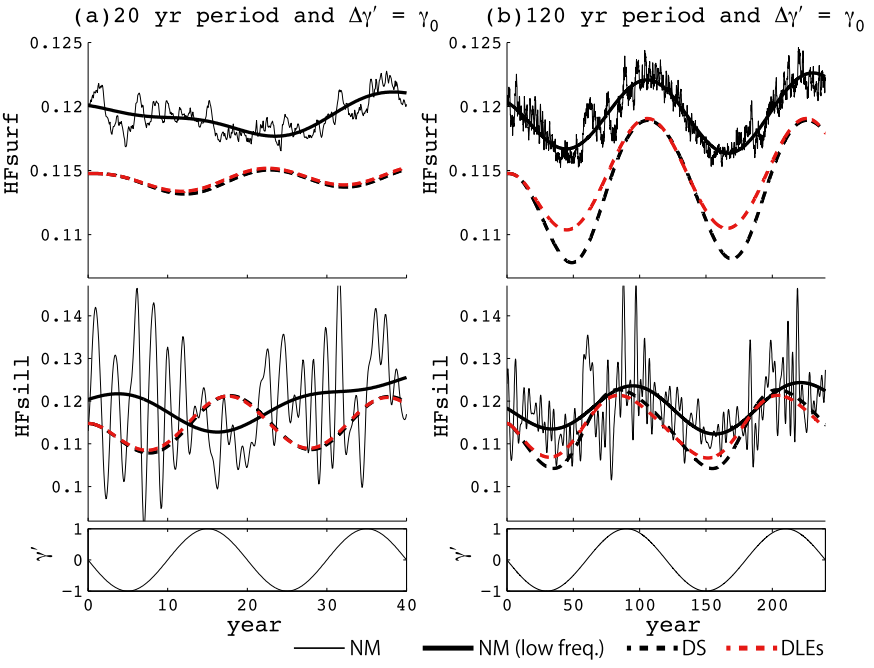

FIG. 12. (a) Time series of (top) HF_{surf}, (middle) HF_{sill}, and (bottom) γ' for the 20-yr periodic precipitation whose nondimensionalized amplitude is γ_0. (b) As in (a), but for the 120-yr periodic precipitation. Thin solid curves are obtained from the NM, and thick solid ones are their low-frequency components. Black dashed curves are obtained from the DS, while red ones are from the DLEs. The thin solid curves of HF_{sill} are obtained by removing components with frequencies higher than $2\pi/(1\,\text{yr})$ in (a) and $2\pi/(3\,\text{yr})$ in (b), while such filters are not used for the thin solid curves of HF_{surf}. The γ' amplitude is normalized to unity.

The HF_{sill} phases are smaller than those of HF_{surf} in all cases (Figs. 13c,d), where the averaged differences are about 0.1 in the model and 0.2 in the DS. This fact means that HF_{surf} is maximal after the HF_{sill} maximum, as predicted by the DS in section 2c.

The difference between HF_{sill} and HF_{surf} changes the temperature in the interior [see (17)]. A large difference between them indicates that much of the inflowing heat is used to change the temperature of the convective water rather than being lost to the atmosphere. According to the DS prediction, this difference is large as a precipitation period is shorter. Amplitudes of $HF_{sill} - HF_{surf}$ from the numerical model, normalized by the respective HF_{sill} amplitudes, are plotted against precipitation periods in Fig. 13e. In all cases, the normalized amplitude of $HF_{sill} - HF_{surf}$ tends to increase as the period decreases, meaning that the fraction of heat lost to the atmosphere decreases. Thus, although there is a lot of scatter in the data, the numerical simulations support the DS prediction that, as a precipitation period decreases, more of the heat flowing into the basin is used to change the temperature of the convective water rather than being lost to the atmosphere. This result suggests that a temporal and rapid change in freshwater input (possibly including sea ice melt and river inflow) does not largely affect the heat flux to the atmosphere, even if the change in precipitation is large. To make a precise estimate of the effect on the atmosphere, the relation between the precipitation time scale and the two relaxation time scales (τ_T and τ_S) needs to be examined for each particular case.

4. Summary

In the present paper, we extended the dynamical system (DS) proposed by Spall (2012) to cases with time-dependent precipitation. The DS predicts the differences in temperature and salinity between the interior and the boundary current in the idealized marginal sea (Fig. 1). There are three inherent time scales derived from the DS: relaxation time scales for temperature and salinity and a precipitation time scale. The relaxation time scales are given by a steady solution of the DS with steady precipitation. The relaxation time scale for temperature τ_T is always smaller than that for salinity τ_S as in Wahlin and Johnson (2009). It is shown here that this time scale difference is due to not only the difference in the form of fluxes at the sea surface but also due to the variation in the eddy transport characterized by the density gradient. For marginal seas of the North Atlantic, such as the Labrador Sea and the Nordic Seas, τ_T is estimated to be about 5 yr

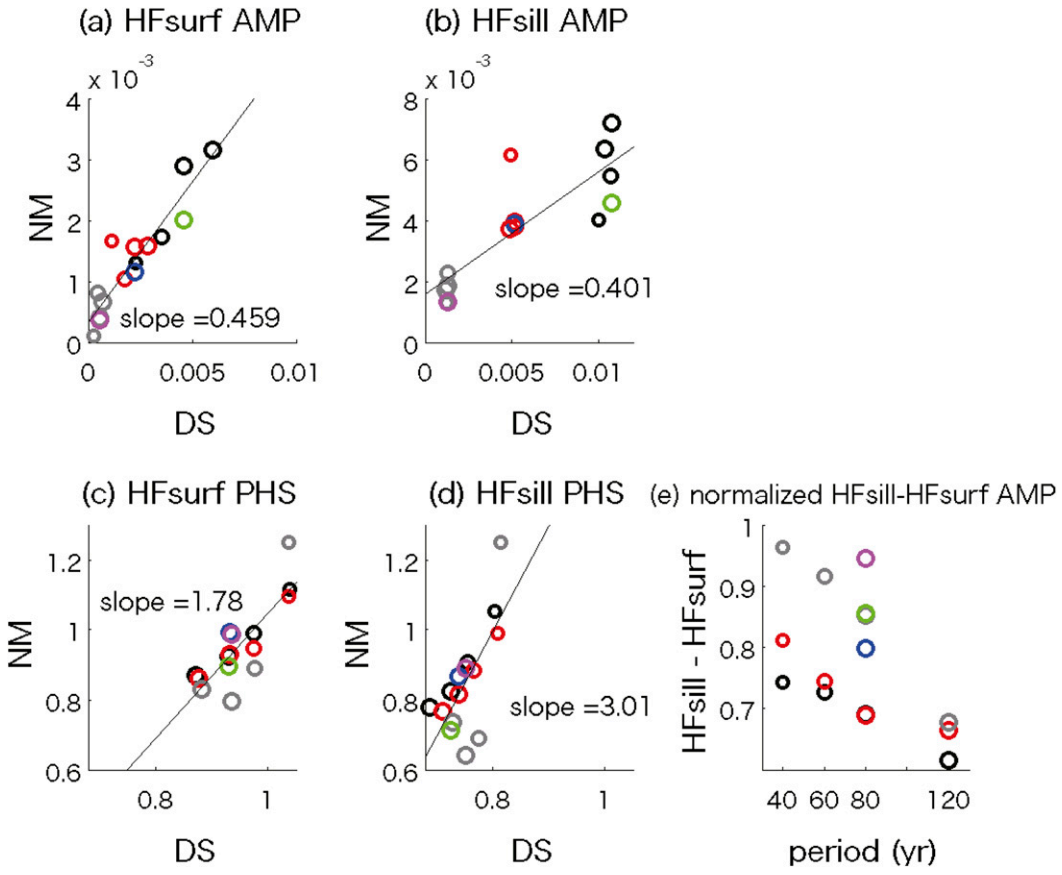

FIG. 13. Comparisons of (a) HF_{surf} amplitude, (b) HF_{sill} amplitude, (c) HF_{surf} phase, and (d) HF_{sill} phase from the NM with those from the DS for sine function precipitation. The line in each figure is obtained by the least squares fitting. Note that the axis ranges in (c) are the same as in (d). (e) Amplitudes of $HF_{sill} - HF_{surf}$ from the numerical model, normalized by respective HF_{sill} amplitudes, are plotted against precipitation periods. A circle in each figure is larger as a precipitation period is longer. Colors used in each figure are denoted in Table 2. A value for the 10- or 20-yr periodic precipitation is not shown in each figure.

while τ_S is about 10 yr. These three time scales together with the precipitation amplitude characterize the DS solution. Because of the coupling between the temperature and salinity equations that results from the baroclinic eddy fluxes (or the variation in the eddy transport), changes in precipitation change not only the salinity of the convective water but also its temperature and heat fluxes. For a precipitation period shorter than the relaxation time scales, the ocean response is relatively weak and one-dimensional, especially for temperature. As the period of precipitation increases, the ocean response becomes strong, while in nondimensional terms the salinity response is generally greater than the temperature response. It was demonstrated that the DS predicts the results from the numerical model qualitatively well over a range of precipitation frequencies and amplitudes, except for temperature in the limit of high-frequency precipitation for which the natural internal variability of the system is larger than the predicted weak-forced response.

Although the numerical model is very idealized, and the DS even more so, the framework provided here may be useful to help distinguish between natural internal variability in the properties of convective water masses and variability that may be forced by low-frequency changes in precipitation. In addition to the predictions of the changes in the temperature and salinity of convective water masses, the DS theory provides the phase relationship between the precipitation, changes in salinity and temperature (which are different), and the changes in heat fluxes both into the basin and into the atmosphere. These phase relationships depend strongly on whether a precipitation period is long or short compared to the relaxation time scales. Because the system is time dependent, all of the changes in the meridional heat flux in the ocean are not transmitted to the atmosphere. For high-frequency forcing (roughly decadal periods or less), most of the changes in the meridional heat flux remain as storage in the deep convective region rather than being lost to the atmosphere.

Acknowledgments. This work was initiated at the 2013 WHOI Geophysical Fluid Dynamics Summer Program, which was supported by the National Science Foundation and the Office of Naval Research. We are grateful to Predrag Cvitanović for discussing how to show that orbits in a dynamical system are limit cycles. We are grateful to the editor and the reviewers for critically reading our manuscript and giving constructive comments. This work was also supported by Grant-in-Aid for Research Fellow (25·8466) of the Ministry of Education, Culture, Sports and Technology (MEXT), Japan, the Program for Leading Graduate Schools, MEXT, Japan (YY), and by the National Science Foundation Grant OCE-1232389 (MAS). Figures 2 and 3 were drawn using the DCL library.

REFERENCES

Born, A., and T. F. Stocker, 2014: Two stable equilibria of the Atlantic subpolar gyre. *J. Phys. Oceanogr.,* **44,** 246–264, doi:10.1175/JPO-D-13-073.1.

Cenedese, C., 2012: Downwelling in basins subject to buoyancy loss. *J. Phys. Oceanogr.,* **42,** 1817–1833, doi:10.1175/JPO-D-11-0114.1.

Gulev, S. K., M. Latif, N. Keenlyside, W. Park, and K. P. Koltermann, 2013: North Atlantic Ocean control on surface heat flux on multidecadal timescales. *Nature,* **499,** 464–468, doi:10.1038/nature12268.

Haney, R. L., 1971: Surface thermal boundary condition for ocean circulation models. *J. Phys. Oceanogr.,* **1,** 241–248, doi:10.1175/1520-0485(1971)001<0241:STBCFO>2.0.CO;2.

Huang, R. X., 1993: Real freshwater flux as a natural boundary condition for the salinity balance and thermohaline circulation forced by evaporation and precipitation. *J. Phys. Oceanogr.,* **23,** 2428–2446, doi:10.1175/1520-0485(1993)023<2428:RFFAAN>2.0.CO;2.

Khatiwala, S., and M. Visbeck, 2000: An estimate of the eddy induced circulation in the Labrador Sea. *Geophys. Res. Lett.,* **27,** 2277–2280, doi:10.1029/1999GL011073.

Lavender, K., R. E. Davis, and W. B. Owens, 2000: Mid-depth recirculation observed in the interior Labrador and Irminger Seas by direct velocity measurements. *Nature,* **407,** 66–69, doi:10.1038/35024048.

Lazier, J. R. N., R. Hendry, A. Clarke, I. Yashayaev, and P. Rhines, 2002: Convection and restratification in the Labrador Sea, 1990–2000. *Deep-Sea Res. I,* **49,** 1819–1835, doi:10.1016/S0967-0637(02)00064-X.

Lilly, J. M., and P. B. Rhines, 2002: Coherent eddies in the Labrador Sea observed from a mooring. *J. Phys. Oceanogr.,* **32,** 585–598, doi:10.1175/1520-0485(2002)032<0585:CEITLS>2.0.CO;2.

——, ——, F. Schott, K. Lavender, J. Lazier, U. Send, and E. D. Asaro, 2003: Observations of the Labrador Sea eddy field. *Prog. Oceanogr.,* **59,** 75–176, doi:10.1016/j.pocean.2003.08.013.

Marshall, J., and F. Schott, 1999: Open-ocean convection: Observations, theory, and models. *Rev. Geophys.,* **37,** 1–64, doi:10.1029/98RG02739.

——, C. Hill, L. Perelman, and A. Adcroft, 1997: Hydrostatic, quasi-hydrostatic, and nonhydrostatic ocean modeling. *J. Geophys. Res.,* **102,** 5733–5752, doi:10.1029/96JC02776.

Pickart, R. S., D. J. Torres, and R. A. Clarke, 2002: Hydrography of the Labrador Sea during active convection. *J. Phys. Oceanogr.,* **32,** 428–457, doi:10.1175/1520-0485(2002)032<0428:HOTLSD>2.0.CO;2.

Rahmstorf, S., 1995: Bifurcations of the Atlantic thermohaline circulation in response to changes in the hydrological cycle. *Nature,* **378,** 145–149, doi:10.1038/378145a0.

——, and Coauthors, 2005: Thermohaline circulation hysteresis: A model intercomparison. *Geophys. Res. Lett.,* **32,** L23605, doi:10.1029/2005GL023655.

Schott, F., M. Visbeck, and J. Fischer, 1993: Observations of vertical currents and convection in the central Greenland Sea during the winter of 1988–1989. *J. Geophys. Res.,* **98,** 14 401–14 421, doi:10.1029/93JC00658.

Send, U., and J. C. Marshall, 1995: Integral effects of deep convection. *J. Phys. Oceanogr.,* **25,** 855–872, doi:10.1175/1520-0485(1995)025<0855:IEODC>2.0.CO;2.

Spall, M. A., 2004: Boundary currents and water mass transformation in marginal seas. *J. Phys. Oceanogr.,* **34,** 1197–1213, doi:10.1175/1520-0485(2004)034<1197:BCAWTI>2.0.CO;2.

——, 2010: Dynamics of downwelling in an eddy-resolving convective basin. *J. Phys. Oceanogr.,* **40,** 2341–2347, doi:10.1175/2010JPO4465.1.

——, 2011: On the role of eddies and surface forcing in the heat transport and overturning circulation in marginal sea. *J. Climate,* **24,** 4844–4858, doi:10.1175/2011JCLI4130.1.

——, 2012: Influences of precipitation on water mass transformation and deep convection. *J. Phys. Oceanogr.,* **42,** 1684–1700, doi:10.1175/JPO-D-11-0230.1.

——, and D. C. Chapman, 1998: On the efficiency of baroclinic eddy heat transport across narrow fronts. *J. Phys. Oceanogr.,* **28,** 2275–2287, doi:10.1175/1520-0485(1998)028<2275:OTEOBE>2.0.CO;2.

Stommel, H., 1961: Thermohaline convection with two stable regimes of flow. *Tellus,* **13A,** 224–230, doi:10.1111/j.2153-3490.1961.tb00079.x.

Straneo, F., 2006: On the connection between dense water formation, overturning, and poleward heat transport in a convective basin. *J. Phys. Oceanogr.,* **36,** 1822–1840, doi:10.1175/JPO2932.1.

Talley, L. D., and M. S. McCartney, 1982: Distribution and circulation of Labrador Sea water. *J. Phys. Oceanogr.,* **12,** 1189–1205, doi:10.1175/1520-0485(1982)012<1189:DACOLS>2.0.CO;2.

van Aken, H. M., M. F. de Jong, and I. Yashayaev, 2011: Decadal and multi-decadal variability of Labrador Sea Water in the north-western North Atlantic Ocean derived from tracer distributions: Heat budget, ventilation, and advection. *Deep-Sea Res. I,* **58,** 505–523, doi:10.1016/j.dsr.2011.02.008.

Visbeck, M., J. Marshall, and H. Jones, 1996: Dynamics of isolated convective regions in the ocean. *J. Phys. Oceanogr.,* **26,** 1721–1734, doi:10.1175/1520-0485(1996)026<1721:DOICRI>2.0.CO;2.

Wahlin, A. K., and H. L. Johnson, 2009: The salinity, heat, and buoyancy budgets of a coastal current in a marginal sea. *J. Phys. Oceanogr.,* **39,** 2562–2580, doi:10.1175/2009JPO4090.1.

Walin, G., G. Broström, J. Nilsson, and O. Dahl, 2004: Baroclinic boundary currents with downstream decreasing buoyancy: A study of an idealized Nordic Seas system. *J. Mar. Res.,* **62,** 517–543, doi:10.1357/0022240041850048.